

REDO SIMULATING DWARF GALAXY EVOLUTION WITH INDIVIDUAL STAR FEEDBACK AND CHEMICAL EVOLUTION I: METHODS AND TEST CASE

ANDREW EMERICK,^{1,2} GREG BRYAN,^{1,3} AND MORDECAI-MARK MAC LOW^{2,1}

¹*Department of Astronomy, Columbia University, New York, NY, 10027, USA*

²*Department of Astrophysics, American Museum of Natural History, New York, NY, USA*

³*Center for Computational Astrophysics, Flatiron Institute, 162 5th Ave, New York, NY, 10003, U.S.A*

ABSTRACT

Saving this for after the first iteration

Keywords: Galaxy – Hydrodynamics – Simulation – Feedback

1. INTRODUCTION

Cosmological simulations of galaxy evolution have shown increasing agreement with observations over the past decade. Recent works have been able to well capture the star forming main sequence, the stellar mass to halo mass relationship, mass metallicity relationship, etc. (e.g. Schaye et al. 2015; Vogelsberger et al. 2014; Genel et al. 2014; Hopkins et al. 2014; Davé et al. 2017) across a wide range of galaxy masses. On small scales, simulations have been able to resolve the long standing disagreement between Λ CDM cosmology and observed galaxies on the low-mass end without invoking new physics beyond Λ CDM. This includes the missing satellites problem (Moore et al. 1999; Klypin et al. 1999), too big to fail (Boylan-Kolchin et al. 2011, 2012; Garrison-Kimmel et al. 2014), and the observed coring of inner dark matter profiles (e.g. Oh et al. 2011). See both Somerville & Davé (2015) and Naab & Ostriker (2016) for recent reviews on these topics.

These simulations generally owe their successes to a combination of better accounting of the baryonic physics that governs galaxy evolution and higher resolution. In particular, a detailed accounting of both multi-channel stellar feedback processes and AGN has shown significant promise over schemes that include supernovae alone, albeit at much greater computational expense. In spite of this progress, practical considerations still limit large cosmological simulations to using sub-grid, phenomenological feedback models, often tuned to reproduce observed galaxy relationships. For this reason, we still have yet to arrive at a complete, self-consistent picture of how feedback governs galaxy evolution.

[I might start intro here]

Due to its complexity, the detailed interstellar medium (ISM) and chemical abundance properties, beyond total metallicity, are sensitive tests of the underlying physical processes that govern galaxy evolution. Examining these in more detail in galaxy scale simulations is an important and exciting new discriminator between models. There is a considerable body of work examining the chemodynamical evolution of galaxies using cosmological hydrodynamics simulations (e.g. Lia et al. 2002; Kawata & Gibson 2003; Kobayashi 2004; Tornatore et al. 2004; Romeo et al. 2005; Oppenheimer & Davé 2008; Wiersma et al. 2009; Shen et al. 2010; Stinson et al. 2010; Guedes et al. 2011; Brook et al. 2014; Snaith et al. 2015; Oppenheimer et al. 2016; Schaye et al. 2010, 2015; Hopkins et al. 2014). These simulations, coupled with additional attention to feedback processes, have made remarkable progress in reproducing global galaxy trends such as evolution of the mass-metallicity relationship (e.g. Obreja et al. 2014; Ma et al. 2016a; Davé et al. 2017) and more detailed quantities such as metallicity distribution functions (MDFs) and abundance evolution of individual species (Marcolini et al. 2008; Revaz et al. 2009; Sawala et al. 2010; Revaz & Jablonka 2012; Jeon et al. 2017; Hi-

[I don't know that we're avoiding metal mixing issues, just using a different numerical mixing scheme. Without an explicit viscosity modeling subgrid turbulence, we're still mixing at a rate determined by grid viscosity, which is not even necessarily constant with an AMR grid.]

rai & Saitoh 2017). However, there is a general lack of numerical diversity in these works, as a majority are implemented in some flavor of smooth particle hydrodynamics (SPH) schemes. Given the known differences between hydrodynamics implementations (Agertz et al. 2007; Kim et al. 2014, 2016), extending these models to a grid-based code is a valuable and complementary approach towards investigating galactic chemical evolution that has only been done recently (Few et al. 2012, 2014; Vorobyov et al. 2015). Additionally, grid-based schemes are able to generally avoid issues with metal mixing, one of the largest model uncertainties in standard SPH codes.

The native SPH scheme is incapable of capturing mixing between chemically inhomogeneous particles, as necessary for chemical evolution. This must be handled through sub-grid models of turbulent metal diffusion (e.g. Shen et al. 2010, 2013; Brook et al. 2014; Su et al. 2017) which, while sophisticated, must still generally be fine-tuned. Even more, a given parameterization is not necessarily applicable generally (Revaz et al. 2016), though recent studies have shown great improvements to this end (Escala et al. 2017). Metal mixing efficiencies may also vary species-by-species (refs), as suggested by recent work (e.g. Cohen et al. 2013; Roederer et al. 2014; Frebel & Norris 2015; Hirai & Saitoh 2017; Côté et al. 2017). In part, this is because mixing behavior is tied critically to the feedback source (stellar winds, supernovae, and possibly more exotic sources) in which they are injected to the ISM. The variations in how one handles sub-grid metal injection and metal mixing schemes can lead to challenges in connecting models back to the fundamental physics that drives galactic evolution. We seek to produce a complementary approach to studying galactic chemical evolution with a new chemical evolution scheme implemented in the adaptive mesh refinement code Enzo designed for high resolution simulations of isolated galaxies.

Although increasing physical resolution reduces one's reliance on sub-grid physics, at high particle mass resolution ($M \lesssim 10^3 M_\odot$) standard schemes for modeling stars as simple stellar populations (SSPs) (as studied in detail in Revaz et al. 2016) do not make physical sense. Below $10^4 M_\odot$, SSPs begin to no longer fully sample the IMF, and can no longer be considered average representations of stellar populations; this becomes conceptually problematic at SSP masses comparable to or below the mass of the most massive star ($\sim 100 M_\odot$). Various approaches exist to address this issue (e.g. Kobayashi et al. 2000; Weidner & Kroupa 2004; Pflamm-Altenburg & Kroupa 2006; Revaz & Jablonka 2012; Rosdahl et al. 2015; Kroupa et al. 2013), but none are without caveats (Revaz et al. 2016), save for schemes which begin to track the star-by-star information within a given particle by directly sampling the IMF at formation time (e.g. Hu et al. 2017). Perhaps the most naive solution, though untenable for large

scale simulations, is to remove the SSP formalism and track stars as individual particles. In this work, we follow stars as individual star particles, allowing us to place unprecedented detail on our accounting of stellar feedback processes and chemical enrichment.

The relative simplicity of idealized, isolated galaxy evolution simulations allows for a focused, first-principles approach to studying multi-channel feedback mechanisms. We follow recent work using low mass dwarf galaxies as laboratories to study in detail how feedback governs galaxy evolution. For example, [Forbes et al. \(2016\)](#) found that photoelectric heating can be a significant source of feedback in small galaxies. [Hu et al. \(2016\)](#) and [Hu et al. \(2017\)](#) examined the relative importance of various feedback physics in regulating ISM properties of dwarf galaxies. Our work builds upon our current understanding of feedback and galactic chemo-dynamics while making three notable advancements: 1) direct star-by-star modeling, 2) stellar wind feedback, and 3) using an adaptive ray tracing method to follow stellar ionizing radiation. Using star-by-star modeling, we are able to capture in more detail the stellar yields from individual stars released over their lifetime. In addition to better capturing how individual metal species enrich the ISM, this allows us to chemically tag individual stars. This opens an exciting new channel for testing models of galaxy evolution by enabling us to leverage current and ongoing observations probing the detailed chemical abundances of stars in the Milky Way and Local Group, such as APOGEE and APOGEE2 ([Majewski et al. 2010, 2016](#)), the Gaia-ESO survey ([Gilmore et al. 2012](#)), and GALAH ([De Silva et al. 2015](#)).

This paper is the first in a series of papers examining in detail the role that the individual components of multi-channel stellar feedback play in galaxy dynamical and chemical evolution. In this paper we introduce a new method of modeling for feedback physics and galactic chemical enrichment in the cosmological, hydrodynamics code `Enzo`. For the first time in galaxy-scale simulations, we model star formation down to particles representing individual stars, while simultaneously capturing stellar feedback through stellar winds, core collapse and Type 1a supernovae, photoelectric heating, and ionizing radiation through ray-tracing radiative transfer. In addition, we couple to a self-consistent set of stellar yields tables from the to track stellar yields from massive star stellar winds, AGB star winds, and supernovae. We describe each mode of our multi-channel feedback implementation in detail below, and briefly discuss their implementation in an isolated dwarf galaxy simulation.

Readers who may want to only briefly skim (or skip) over the details of our included physics are advised to just read the beginning of Section 2, which contains a complete – yet brief – summary of the included physics.

[didn't
Hu+ end
up disagreeing?]

2. METHODS

In brief, we produce high resolution galaxy scale simulations tracking stars not as SSP's, but as individual stars sampled from an assumed IMF. This allows us to follow star-by-star variations in feedback physics and stellar yields in detail. To properly model the ISM, we track non-equilibrium primordial chemistry (including molecular hydrogen) using `Grackle` ([Smith et al. 2017](#)), with heating and approximate self-shielding from a metagalactic UV background. We use updated `Cloudy` metal line cooling tables consistent with our self-shielding approximation (see Appendix D), and an updated observationally motivated dust model for the low metallicity regimes studied here ($Z \lesssim 0.1 Z_{\odot}$). Each star is assigned basic properties (surface gravity, effective temperature, radius, lifetime) from tabulated stellar evolution models, which inform how the stars deposit their feedback. We directly track ionizing radiation from massive stars using an adaptive ray tracing radiative transfer method that includes the effects of radiation pressure. In addition, we follow the optically thin non-ionizing UV radiation from these stars leading to photoelectric heating and Lyman-Werner (LW) dissociation of molecular hydrogen. We track the stellar wind feedback and supernovae from these stars, depositing individual metal yields from both. We include AGB wind feedback and yields for lower mass stars, and track these directly as Type Ia supernovae progenitors. We follow yields for 15 individual metal species (C, N, O, Na, Mg, Si, S, Ca, Mn, Fe, Ni, As, Sr, Y, and Ba), chemically tagging each star with the associated local gas abundances for each species. These methods are discussed in full detail below.

2.1. Hydrodynamics and Gravity

We use the adaptive mesh refinement (AMR) hydrodynamics and N-body code `Enzo`¹ to simulate the chemodynamical evolution and detailed feedback physics in a set of high resolution, isolated, low mass dwarf galaxies. `Enzo` is an open-source code that is undergoing continual, active development by many researchers across several institutions. We use a substantially modified version of the current development version of `Enzo` (version 2.X) in this work.² We solve the equations of hydrodynamics using a direct-Eulerian piecewise parabolic method ([Colella & Woodward 1984; Bryan et al. 1995](#)) and a two-shock approximate Riemann solver with progressive fallback to more diffusive Riemann solvers in the event that higher order methods produce negative densities or energies. We compute the total gravitational potential from gas self-gravity, stars, and static back-

¹ <http://www.enzo-project.org>

² This version is contained in a publicly available fork of the main repository: <https://bitbucket.org/aemerick/enzo-emerick>. Specifically, simulations presented here were conducted at changeset 445de816fd99.

ground dark matter potential. The collisionless star particles are evolved with a particle-mesh N-body solver at an effective force resolution of $\sim 2\Delta x$, where Δx is the local cell size.

The computational domain in an AMR simulation is adaptively refined up to a designated resolution limit for a given set of refinement criteria. We require that the Jeans length be resolved by a minimum of 8 cells, continually refining a given region until this criteria is met or the region reaches the maximum resolution. Our maximum resolution in the simulations presented here is 1.8 pc. At maximum resolution, the Jeans length can become under resolved, leading to artificial numerical fragmentation. Studies have shown that resolving the Jeans length by at least 4 cells is required to suppress this fragmentation (Truelove et al. 1997).

We set the star formation density threshold to the point which the Jeans length becomes resolved by only 4 cells in sub-200 K gas, or about 200 cm^{-3} (as discussed further in Section 2.3). Forming stars from this gas will reduce the local density, ensuring the Jeans length is resolved. However, since star formation is not instantaneous, we employ a pressure floor to support gas against artificial collapse once its Jeans length becomes unresolved. This prevents dense, self-gravitating gas from rapidly reaching densities significantly above our resolution limit. The use of a pressure floor is common in galaxy scale simulations with limited dynamic range. (**I contrasted this to Hu's work which allows arbitrarily high densities, hoping feedback mitigates how high the densities actually get, but took it out. Leave it in?**)

2.2. Chemistry and Cooling Physics

We use the chemistry and cooling library `Grackle`³ v 3.0 to follow a nine species non-equilibrium chemistry network (H, H⁺, He, He⁺, He⁺⁺, e⁻, H₂, H⁻, and H₂) which includes radiative heating and cooling from these species and metals.⁴ `Grackle` is a freely available, open source multi-code library, designed to interface with a wide variety of astrophysical codes. We outline specific model choices made in our simulations and refer the reader to (Smith et al. 2017) for a detailed discussion of the code. We apply the Glover & Abel (2008) three body rate for H₂ formation and include a model for H₂ formation on dust, dust heating, and dust cooling following the methods in Omukai (2000) and Omukai et al. (2005) as included in `Grackle`. However, we update the default dust to gas ratio scaling in `Grackle` to account for the steeper scaling in low metallicity regimes ($Z \lesssim 0.1Z_{\odot}$) with the broken power law scalings from Rémy-Ruyer et al.

³ <https://grackle.readthedocs.io/en/grackle-3.0/>

⁴ We use a slightly modified version of the the main `Grackle` repository, available at <https://bitbucket.org/aemerick/grackle-emeric> at changeset 59adc76b3130.

(2014). For metallicities above $\sim 0.1Z_{\odot}$, this is equivalent to the the default behavior of `Grackle`, where dust content scales linearly with metallicity.

Metal line cooling is modeled using pre-computed Cloudy⁵ tables interpolated as a function of density, temperature, and redshift, using the Haardt & Madau (2012) UV metagalactic background. As discussed in more detail in Section 2.5.6, we account for approximate self-shielding of H and He against this UV background. Using this prescription with metal line cooling tables computed under an optically thin assumption can lead to an order of magnitude overestimation of the cooling rate at certain densities. To address this issue, we use re-computed metal line tables consistent with the self-shielding approximation. We have made these new tables public in the main `Grackle` repository. These are both discussed in greater detail in Appendix D.

2.3. Star Formation Algorithm

In order resolve individual star formation on galaxy scales, we implement a stochastic star formation algorithm adopted from Goldbaum et al. (2015, 2016). Each cell at the maximum refinement level is capable of forming stars if it meets the following local criteria: 1) $n_{\text{cell}} > n_{\text{thresh}}$, 2) $T_{\text{gas}} < T_{\text{thresh}}$, 3) $M_{\text{gas}} > M_{\text{Jeans}}$, and 4) $\vec{\nabla} \cdot \vec{v} < 0$, where n_{thresh} is a resolution dependent density threshold, T_{thresh} is a temperature threshold, and M_{Jeans} is the local Jeans mass. Our fiducial values for n_{thresh} and T_{thresh} are 200 cm^{-3} and 200 K respectively. We limit the fraction of a cell's gas mass that is converted into stars by requiring $M_{\text{gas}} > f_{\text{thresh}} M_{\text{max},*}$, where $f_{\text{thresh}} = 2.0$ and $M_{\text{max},*}$ is the maximum star mass ($100 M_{\odot}$). No star formation occurs when $M_{\text{gas}} < f_{\text{thresh}} M_{\text{max},*}$, ensuring that a star formation episode does not produce negative densities.

We make the common ansatz that star formation occurs by converting some fraction of gas into stars in a free fall time (τ_{ff}) as characterized by a star formation efficiency, $\epsilon_f \simeq 0.02$. At high resolution, one's choice of ϵ_f should be irrelevant (Orr et al. 2017; Hopkins et al. 2017), as star formation is ultimately self-regulated by feedback. The the gas mass converted to stars in a time step, dt , is

$$M_{\text{gas} \rightarrow *} = \epsilon_f M_{\text{gas}} \frac{dt}{\tau_{\text{ff}}}. \quad (1)$$

In practice, $dt/\tau_{\text{ff}} \ll 1$, and $M_{\text{gas} \rightarrow *}$ is smaller than the minimum star particle mass at parsec scale resolution. We therefore allow star formation to proceed stochastically, following the methods in Goldbaum et al. (2015, 2016), modified for variable stellar masses. In each cell that could potentially form stars, we compute the probability that $100 M_{\odot}$ of gas will be converted into stars in that time step, and use a ran-

⁵ <http://www.nublado.org/>

dom number draw to determine whether or not star formation actually occurs. If it does, we random sample over the adopted IMF until $100 M_{\odot}$ of stars form, keeping last sampled particle if the total stellar mass formed exceeds $100 M_{\odot}$. We make the simple assumption of a Salpeter IMF (Salpeter 1955) with $\alpha = 2.35$, sampling over a minimum stellar mass of $1 M_{\odot}$ and maximum stellar mass of $100 M_{\odot}$.

Formed stars are deposited with random positions within the star forming cell and assigned velocities equal to the cell bulk velocity with a 1 km s^{-1} velocity dispersion. Stars are assigned metallicities corresponding to the metallicity of the star forming zone, and are chemically tagged with 17 individual species abundances (H, He, and the 15 metals) we follow in our simulations. Stars evolve throughout the simulation, losing mass from stellar winds and supernovae as described below, and by changing types, but persist throughout the entire simulation. For example, low mass stars are tagged as white dwarfs at the end of their life, which may eventually explode as a Type Ia supernova (discussed below), after which they persist as massless tracer particle “remnants”.

Finally, each star is marked as a “must refine” particle, requiring that each star be surrounded by a four-cell region at the highest level of refinement. This ensures that both stellar winds and supernovae feedback are maximally resolved, and that any ejected yields are deposited over a consistent physical scale throughout the simulation.

2.4. Stellar Properties

Given their birth mass and metallicity, we interpolate over the PARSEC grid of stellar evolution tracks (Bressan et al. 2012) to assign a lifetime and AGB phase start time (if any) to each star, as well as an effective temperature (T_{eff}) and surface gravity (g), used in computing radiation properties (see Section 2.5.5). We use the largest subset of the PARSEC models that are regularly sampled in our mass/metallicity space of interest, with 26 mass bins over $M_* \in [0.95, 120.0] M_{\odot}$ and 11 metallicity bins over $Z \in [10^{-4}, 0.017]$. Although T_{eff} and g evolve over time for stars, modifying stellar radiative properties, following a stellar evolution track for each of our stars is beyond the scope of this work. We instead fix these properties at their zero age main sequence values.

2.5. Stellar Feedback and Chemical Yields

2.5.1. Stellar Yields

For the first time in galaxy scale simulations, we track galactic chemodynamical evolution using stellar yields as ejected from star particles that represent individual stars. We adopt the NuGrid⁶ collaboration’s set of stellar yields given on a uniformly sampled grid in stellar mass and metallicity

with 12 mass bins over $M_* \in [1.0, 25.0] M_{\odot}$ and five metallicity bins at $Z = 0.02, 0.01, 0.006, 0.001$, and 10^{-4} (Pignatari et al. 2016; Ritter et al. 2017). This grid includes yields from the AGB phase of stars between 1 and $7 M_{\odot}$, as well as yields from both stellar winds and core collapse supernova of massive stars over 12 to $25 M_{\odot}$. We compliment these tables to track stellar winds for stars more massive than $25 M_{\odot}$ using tables from Slemer et. al. (in prep), based on the PARSEC stellar evolution tracks (Bressan et al. 2012; Tang et al. 2014); we ignore supernovae yields from these stars (see below). We combine all stable isotope yields for a given element into a single elemental abundance for all stable elements from hydrogen to bismuth. Although we can follow an arbitrary number of metal species, practical considerations prevent this in any given simulation. We refer the reader to previous uses of the NuGrid yields in one zone galactic chemical enrichment models (Côté et al. 2016a,b, 2017) for a detailed discussion on how various model uncertainties can influence galactic chemical evolution.

Above some mass, M_{trans} , within the unsampled range of 7 to $12 M_{\odot}$ stars do not undergo AGB wind phases and end their lives as core collapse supernovae. Where this transition occurs is uncertain, but is commonly taken to be around 8 - $10 M_{\odot}$. This is a free parameter in our model, but we take $M_{\text{trans}} = 8 M_{\odot}$ as our fiducial value. In our model, stars below this mass eject their wind yields in an AGB phase only at the end of their lives, typically over a period comparable to or less than a few time steps ($\lesssim 10$ kyr). Stars above this mass eject their stellar yields via “massive” stellar winds at a constant mass loss rate throughout their lifetime, ending their lives as a core collapse supernova (see Section 2.5.2 for details on the wind energetics). Varying M_{thresh} changes both the time at which yields for stars around this mass are ejected (for reference, the lifetime of a $8 M_{\odot}$ star is about 35 - 40 Myr), and the energy injection from these winds. Côté et al. (2017) explores how one’s choice of M_{thresh} affects galaxy abundances in a one-zone model.

There are large uncertainties in stellar yields for stars more massive than $25 M_{\odot}$ (see Côté et al. 2016a, and references therein). Indeed, even the exact fate of these stars is uncertain (e.g. Woosley et al. 2002; Zhang et al. 2008; Ugliano et al. 2012), particularly as a function of metallicity (Fryer et al. 2012) with potentially multiple stable/unstable regimes as a function of mass (Heger et al. 2003). Due to this uncertainty, and to avoid erroneously extrapolating from our yield tables, we adopt the simplest model and assume all stars above $25 M_{\odot}$ end their life through direct collapse to a compact object with no mass or energy ejection.

Type Ia supernova are an important additional source of galactic chemical enrichment. These iron group rich events are responsible for the ~ 1 Gyr timescale turnover, or “knee”, in $[\alpha/\text{Fe}]$ vs $[\text{Fe}/\text{H}]$ diagrams. We use the Type Ia supernova

⁶ <http://www.nugridstars.org>

yields given in Thielemann et al. (1986), adopting a Type Ia supernova model as discussed in Section 2.5.4.

2.5.2. Stellar Winds

Stellar winds are important sources of early (massive stars) and late (AGB stars) enrichment and feedback in galaxies. Although the energy injected via winds over the lifetime of a cluster of stars is much less than that of supernovae and radiation, stellar winds are potentially important sources of pre-supernova feedback. In both AGB phase winds and massive star winds we inject the feedback energy in a 3-cell radius spherical region centered on the emitting star particle assuming full thermalization of the wind kinetic energy. The total injected energy in timestep Δt is therefore $E_{\text{wind}} = \dot{M}\Delta t \times v_{\text{wind}}^2 + E_{\text{th}}$, where E_{th} is the thermal energy of the ejected gas mass ($\dot{M}\Delta t$) given the star's interpolated T_{eff} . We use a monte-carlo sampling method to inject mass and energy into the surrounding cells to account for partial cell overlap at the edge if the injection region that is a result of mapping a spherical injection region to cubic grid cells.

We assume constant mass loss rates for all winds as set by the yields tables and either the lifetime of the star (for massive stars) or the length of the AGB phase (for low mass stars). Massive star stellar winds have typical velocities on order 10^3 km s $^{-1}$ (Leitherer et al. 1992). Satisfying the Courant time step becomes prohibitively expensive following this gas ($dt \sim 100$ yr), particularly as stellar wind bubbles have typical temperatures of 2×10^6 K (Weaver et al. 1977). For this reason, we adopt the common simplification of reducing the wind velocity (e.g Offner & Arce 2015). In our case, we fix massive star stellar winds to $v_{\text{wind}} = 1$ km s $^{-1}$ for stars above $8 M_{\odot}$. Our initial tests show that turning off energy injection from stellar winds does not significantly affect the global star formation rate of our galaxies. Due to the substantial additional computational expense of following stellar winds for Gyr timescales, we reserve examining the detailed importance of winds to future work. These points are discussed in more detail in Section 5.3.1.

Stars that undergo an AGB phase only deposit their feedback at the end of their lives, as determined by the PARSEC evolution tracks. AGB wind velocities vary dramatically over their relatively short lifetimes, but are typically on the order of 10 km s $^{-1}$. For simplicity, we adopt a fixed AGB phase wind velocity of 20 km s $^{-1}$ for all AGB stars.

2.5.3. Core Collapse Supernovae

Stars between $M_{\text{thresh}} = 8 M_{\odot}$ and $25 M_{\odot}$ end their lives as core collapse supernovae, ejecting mass and yields as determined by the NuGrid stellar yield tables at 10^{51} erg of thermal energy. Due to the high resolution (1.5 - 2.5 pc depending on galaxy size) of our simulations, we generally well resolve the Sedov phase of each supernova explosion (see Appendix C). We find injecting thermal energy alone

in a 3 cell radius spherical region around the star particle to be sufficient to resolve the supernovae explosions. We continue to track any remaining stellar mass after the SNe as a massive “remnant” tracer particle. In future work these particles can be used to self-consistently account for more exotic sources of feedback and chemical enrichment through X-ray binaries and neutron-star-neutron-star merger events which, while rare, could be important in long term galaxy evolution. **Should I reference a few recent hydro sims that included these feedback sources? - AE**

2.5.4. Type Ia Supernova

We continue to track low mass stars ($M < 8 M_{\odot}$) after their death as white dwarf (WD) particles, marking a subset as Type Ia supernova progenitors. At the end of their life, we assign a new mass to these particles following the initial to final mass relation of Salaris et al. (2009). **I originally reproduced the equations here, but it is currently commented out. - AE** We follow the common assumption that progenitor stars with masses between 3 and $8 M_{\odot}$ form WD’s that are Type Ia progenitors (see Côté et al. 2017, and references therein). We compute the probability that a given Type Ia progenitor will explode as a function of time using an observationally motivated delay time distribution (DTD) model. The SNIa rate is taken as a power law in time, $\Psi(t) \propto t^{-\beta}$, whose slope and normalization are observables, and η the fraction of stars which can form SN Ia progenitors that *will* explode as a SN Ia within a Hubble time. The value for η depends on the normalization of the DTD (an observable), as well as one’s choice of IMF and mass range of potential SN Ia progenitors (as given above). This fraction is given as

$$\eta = \frac{N_{\text{Ia}}}{M_{\text{SF}}} \frac{\int_{M_{\min}}^{M_{\max}} m(dN/dm)dm}{\int_{M_1}^{M_2} (dN/dm)dm}, \quad (2)$$

where $N_{\text{Ia}}/M_{\text{SF}}$ is the DTD normalization, which represents the fraction of stars that form SN Ia progenitors, M_{\min} and M_{\max} are the lower and upper bounds of the IMF (dN/dm), and M_1 and M_2 are the lower and upper bounds of the range of stars that can form Type Ia candidates. The DTD slope, β , is of order unity, with typical values between 1.0 and 1.2 (see Maoz et al. (2014) for a recent review). $N_{\text{Ia}}/M_{\text{SF}}$ represents the number of SN Ia per mass of star formation; this can be derived by taking observed values of the SNIa rate and integrating over a Hubble time. Typical values for this are on order of $10^{-3} M_{\odot}^{-1}$ (Maoz et al. 2014). We adopt 1.2 Maoz et al. (2010) and $0.8 \times 10^{-3} M_{\odot}^{-1}$ Graur & Maoz (2013) for our fiducial values of β and $N_{\text{Ia}}/M_{\text{SF}}$. Given our choice of IMF, and with $M_{\min} = 1 M_{\odot}$, $M_{\max} = 100 M_{\odot}$, $M_1 = 3 M_{\odot}$, and $M_2 = 8 M_{\odot}$, this gives $\eta = 0.041$.

Finally, the probability a Type Ia candidate will explode at a time t after the formation of its main sequence progenitor is taken as

$$P(t) = \dot{P}(t)dt = \eta \frac{t^{-\beta}}{\int_{t_0}^{t_H+t_0} \tau^{-\beta} d\tau} dt, \quad (3)$$

where t_0 is the formation time of the WD and the denominator normalizes the total probability to η . This naturally accounts for both a prompt and delayed Type Ia supernova population in our simulations. In practice, we invert the cumulative probability distribution to assign an exact time at which a given WD will explode, rather than making a random number draw for every WD particle every time step as η is small.

2.5.5. Ionizing Radiation

Radiation feedback (ionization, ionization heating, and radiation pressure) is an important source of pre-SN feedback in galaxies. HII regions carved out by stellar radiation change the ISM structure where SNe eventually explode, generally increasing their dynamical importance. However, when accounting for angular effects, radiation can also allow energy from SNe to dissipate more readily through channels carved through dense clouds. Radiation feedback effects have been included with various approximations in a wide range of simulations (e.g. Oppenheimer & Davé 2006; Krumholz et al. 2007; Hopkins et al. 2012; Agertz et al. 2013; Renaud et al. 2013; Stinson et al. 2013; Roškar et al. 2014; Ceverino et al. 2014; Hopkins et al. 2014; Agertz & Kravtsov 2015; Forbes et al. 2016; Hu et al. 2016, 2017; Hopkins et al. 2017), with limited application in full radiation hydrodynamics simulations (Wise et al. 2012a,b, 2014; Kim et al. 2013a,b; Pawlik et al. 2013; Rosdahl et al. 2015; Aubert et al. 2015; Ocvirk et al. 2016; Baczynski et al. 2015; Pawlik et al. 2017) due to the additional computational expense of direct ray tracing. As we seek a complete accounting of stellar feedback physics, we follow HI and HeI ionizing radiation from our stars through ray tracing methods described below. In this particular work, we use two different simulations of the same galaxy to demonstrate the importance of following radiation feedback with full radiative transfer methods (see Section 3).

Enzo includes an adaptive ray tracing implementation, ENZO+MORAY (Wise & Abel 2011), to solve the equations of radiative transfer as coupled to the hydrodynamics of the simulation. We follow H I and He I ionizing photons which are coupled to the Grackle primordial chemistry and heating and cooling routines to track photoionization and heating, as well as radiation pressure on hydrogen. Radiation pressure is expected to be an important source of feedback only in more massive galaxies; we explore this point further in this work.

We adopt the H I and He I ionizing photon rates for each star using the OSTAR2002 (Lanz & Hubeny 2003) grid of O-type stellar models, appropriate for $M_* \gtrsim 15 M_\odot$ at solar metallicity⁷. We use linear interpolation in stellar effective temperature, surface gravity, and metallicity to compute the ionizing photon fluxes and rates for each star. Stars less massive than about $15 M_\odot$ are generally off of the OSTAR2002 grid, and massive stars with sub-solar metallicity generally have effective temperatures above the OSTAR2002 grid. In this case, we integrate a black body spectrum at T_{eff} to obtain the ionizing photon fluxes, but normalize the result to be continuous with the OSTAR2002 grid (see Appendix B). (Dale et al. 2012) demonstrated that uncertainties on order of a few in the ionizing radiation rates are not significant in giant molecular cloud (GMC) scale simulations.

Instead of assigning a fixed ionizing photon energy across all sources, we integrate over each star’s blackbody curve to compute the average ionizing photon energy individually for each source (see Appendix B). The average energy for H I and He I ionizing photons changes significantly over the OSTAR2002 temperature range ($\log(T_{4,\text{eff}}[K]) \in [2.75, 5.5]$), ranging from 15.72 eV to 20.07 eV and 26.52 eV to 31.97 eV respectively.

We also include the effects of radiation pressure on HI. This has been shown to be important in suppressing the star formation rates of dwarf galaxies by influencing turbulence and the dense gas content of the ISM (Wise et al. 2012a; Ceverino et al. 2014). We ignore the absorption of ionizing radiation by dust and re-radiation in the infrared. This is included in other models (e.g. Rosdahl et al. 2015; Hopkins et al. 2014, 2017) as this may increase by a factor of a few to several the effective radiation pressure (Zhang & Davis 2017). However, the importance of multiple scattering is still unclear. Other works have shown the effect to only increase the radiation pressure by a factor on order of unity (Krumholz & Thompson 2012; Krumholz 2013). Due to these uncertainties, and given that we focus on low metallicity dwarf galaxies with low dust content, we ignore this effect.

2.5.6. Diffusive Heating

We include two forms of diffusive heating in our simulations, each tied directly to the non-equilibrium primordial chemistry network in Grackle: 1) the optically thin, metagalactic UV background Haardt & Madau (2012), and 2) localized photoelectric (PE) heating from the far-ultraviolet (FUV, $6 \text{ eV} < h\nu < 13.6 \text{ eV}$) radiation from our stars. Photoelectric heating can be a dominant heating mechanism in the ISM (Parravano et al. 2003) of the Milky Way, and could be significant in regulating star formation in dwarf galaxies

⁷ The exact stellar mass range on the OSTAR2002 grid is model dependent and a function of metallicity

(Forbes et al. 2016). However, this conclusion warrants further research as its exact importance in dwarf galaxies relative to other feedback mechanisms is contended (Hu et al. 2016, 2017). Generally, models for PE heating and LW radiation in hydrodynamic simulations of galaxies adopted a constant value or a static, radial profile. Only recently has the localization and time variation of these processes been considered.

Self-shielding of gas against the metagalactic UV background is important in high resolution simulations, particularly for low-mass, low metallicity dwarf galaxies where the UV background is capable of gradually photoevaporating unshielded gas from the galaxy. We have implemented the Rahmati et al. (2013) approximate self-shielding method in `Grackle` to account for HI self-shielding against the UV background (see (Smith et al. 2017) for more details of this implementation). We assume HeI ionization generally follows HI. This allows us to approximate HeI self-shielding using the same form (A. Rahmati, private communication). We ignore HeII photoionization from the UV background entirely. Accounting for self-shielding in this manner leads to an inconsistency in using tabulated, optically-thin metal line cooling rates from Cloudy (see Section 4.1.1 of Hu et al. (2017)). As mentioned previously, we have re-computed metal line cooling tables using Cloudy models of optically thick clouds to be consistent with our self-shielding prescription. This is described in more detail in Appendix D.

We assume the FUV luminosity for each our stars is everywhere optically thin. The FUV flux in each cell is summed over contributions from each star. We parameterize the local photoelectric heating rate following Bakes & Tielens (1994), Wolfire et al. (2003), and Bergin et al. (2004), where

$$\Gamma_{\text{pe}} = 1.3 \times 10^{-24} \epsilon n_{\text{H}} G_{\text{eff}} D \text{ [erg s cm}^{-3}\text{]} \quad (4)$$

where ϵ is an efficiency factor that depends on $G_{\text{o}} T^{1/2} / n_{\text{e}}$, the attenuated local FUV flux

$$G_{\text{eff}} = G_{\text{o}} \exp(-1.33 \times 10^{-21} D N_{\text{H}}), \quad (5)$$

D is the dust to gas ratio, normalized to the solar value, and G_{o} is the local FUV flux normalized to the solar neighborhood (Habing 1968). Aside from a different treatment of D and the attenuation, both discussed below, this is equivalent to the method used in Hu et al. (2016) and Hu et al. (2017).

D is computed consistently with our `Grackle` dust model, using the broken power law fit from Rémy-Ruyer et al. (2014) (see Section 2.2). The extremely low dust to gas ratio in our modeled galaxies leads to a reduction in the photoelectric heating rate by approximately two orders of magnitude, as compared to a model that assumes a D that scales linearly with metallicity at very low metallicity. At these low metallicities, the FUV field only becomes optically thick at length scales of ~ 100 pc for densities of $n \sim 10^2$

cm^{-3} . Given that the ambient density of the ISM is generally $1 - 10 \text{ cm}^{-3}$, we can safely assume the FUV field to be optically thin. However, we do include a localized attenuation prescription which may influence high density or metal enriched regions of the galaxy. We approximate N_{H} given in the equation above locally, as $n_{\text{H}} \Delta x$, where Δx is the cell width; this approximation is necessarily resolution dependent, but substantially more computationally efficient than direct ray tracing.

Properly computing ϵ in Eq. 4 requires an accurate account of the electron number density (n_{e}). This is non-trivial in dense, neutral regions where n_{e} is dominated by contributions from carbon, dust, and PAH ionizations; each of which are not followed directly in these simulations. Instead, we use a log-linear fit of ϵ as a function of n_{H} from the Wolfire et al. (2003) model of Γ_{pe} in the solar neighborhood (see Figure 10b of that work); we adopt $\epsilon = 0.0148 n_{\text{H}}^{0.235}$.

2.5.7. Lyman-Werner Radiation

In addition to the LW radiation from the UV background, we account for localized LW flux from each of our stars to compute the total, local H_2 dissociation rates. Given the local LW flux, the H_2 dissociation rate is taken as $k_{\text{diss}} = \sigma_{\text{H}_2} F_{\text{LW}}$, where σ_{H_2} is the H_2 dissociation cross section. We account for approximate H_2 self-shielding against these sources of LW flux by implementing the Sobolev-like approximation from Wolcott-Green et al. (2011) in `Grackle`.

3. GALAXY INITIAL CONDITIONS

The galaxy presented in this work is constructed to be similar to the observed properties of the Local Group dwarf galaxy Leo P (Giovanelli et al. 2013; McQuinn et al. 2013, 2015a,b), but is not intended to be a matched model to this galaxy. Leo P is gas rich ($M_{\text{gas}} > M_*$) and low metallicity, with $M_{\text{HI}} = 8.1 \times 10^5 \text{ M}_{\odot}$ and $M_* = 5.6_{-1.9}^{+0.4} \times 10^5 \text{ M}_{\odot}$ (McQuinn et al. 2015a) extending to a radius $r_{\text{HI}} = 500$ pc, and with $12 + \log(\text{O/H}) = 7.17 \pm 0.04$ (Skillman et al. 2013), or $Z \sim 5.4 \times 10^{-4}$ adopting $Z_{\odot} = 0.018$ from Asplund et al. (2009). Our dwarf galaxy is constructed without an initial background stellar population, with a total gas mass of $1.8 \times 10^6 \text{ M}_{\odot}$ (or $M_{\text{HI}} = 1.35 \times 10^6 \text{ M}_{\odot}$) and $Z = 4.3 \times 10^{-4}$, comparable to the average $z=0$ metallicity from the stellar models computed in (McQuinn et al. 2015b).

The galaxy initially consists of a smooth, exponential gas disk in hydrostatic equilibrium with a static, background dark matter potential. The gas profile follows Tonnesen & Bryan (2009) and Salem et al. (2015), or

$$\rho_{\text{gas}}(R, z) = \frac{M_{\text{gas}}}{2\pi a_{\text{gas}}^2 b_{\text{gas}}} 0.5^2 \operatorname{sech} \left(\frac{R}{a_{\text{gas}}} \right) \operatorname{sech} \left(\frac{z}{b_{\text{gas}}} \right) \quad (6)$$

where a_{gas} and b_{gas} are the radial and vertical gas disk scale heights, and M_{gas} is approximately 70% of the total gas mass.

We set $a_{\text{gas}} = 250$ pc, $b_{\text{gas}} = 100$ pc, and a total gas mass of $M_{\text{T,gas}} = 2.0 \times 10^6 M_{\odot}$. We adopt a Burkert [Burkert \(1995\)](#) dark matter potential with $M_{\text{vir}} = 3.5^8 M_{\odot}$, $R_{\text{vir}} = 14.3$ kpc and $r_s = 370$ pc. This gives a maximum circular velocity $V_{\text{max}} = 17.4$ km s $^{-1}$ at $R_{\text{vmax}} = 1.2$ kpc. These parameters were adopted specifically to match the observed dynamical mass of Leo P interior to 500 pc, or $M_{\text{dyn}}(r < 500 \text{ pc}) = 2.7 \times 10^7 M_{\odot}$, and represent virial properties near the minimum halo mass expected for galaxies of this size ([Ferrero et al. 2012](#)) (need more cite). We will explore the effect of adopting different dark matter potentials within the large range of possible profiles in a future work.

Following the initialization procedure of [Hu et al. \(2017\)](#), we use artificial supernova driving to generate realistic densities and turbulent properties in the galaxy ISM. This additionally prevents an otherwise uniform collapse of the gas disk. The supernovae explode at a fixed rate of 0.4 Myr $^{-1}$, corresponding to the SFR obtained given the central HI surface density and the relation presented in ([Roychowdhury et al. 2009](#)). We stop the artificial driving 25 Myr after the first star particle forms. These artificial supernova do not drive chemical evolution of the galaxy; their metal yields correspond to the mean ISM abundances.

4. RESULTS

We present our initial results here, providing a brief overview of the morphological (Section 4.1), star formation (Section 2.3), ISM (Section 4.3), radiation field (Section 4.4), outflow (Section 4.5), and chemical (Section 4.6) properties of our dwarf galaxy during the first **200 Myr** after the first star forms. Our analysis makes extensive use of the open-source YT toolkit ([Turk et al. 2011](#)).⁸

4.1. Morphological Structure and Evolution

We begin by characterizing the morphological properties of our dwarf galaxy, as demonstrated in a series of face-on and edge-on images, presented in Figure 1 and Figure 2. Each figure gives density weighted projections of number density (first row), temperature slices (second row), HI column density projections (third row), and O column density projections (fourth row), at four different times in the simulation (*list times here*). In addition, the number density plots show all main sequence stars in the simulation at the given time, represented by individual black points. Towards the end of the simulation time, the half light radius is 389 ± 21 pc, where the uncertainty represents the 1σ variation in this quantity during the final 20 Myr.

⁸ All analysis scripts used in this work can be found at <https://github.com/aemeric/galaxy-analysis> at changeset **changeset number**.

The increased gravitational potential towards the center of our dwarf galaxy leads to an inside-out star formation evolution, whereby star formation propagates from the inner regions outward during the galaxy's evolution. This is obvious in the face-on panels, which demonstrate the growth of the stellar population from the center outward, and the declining gas densities inside-out as a result of stellar feedback driven winds. This region quickly becomes volume-filled with both warm and hot gas generated from radiation feedback and supernovae respectively. Both the ISM and the halo gas is multi-phase, containing gas at cold, warm, and hot temperatures with a range of densities, as evident by the temperature slices in both panels. The ISM properties are quantified further in Section 4.3.

The gas disk is thin outside the stellar radius of our galaxy, but is resolved at all radii. In Figure 3 we plot the scale height of our gas disk as a function of radius averaged over the last 20 Myr of simulation time (black), at the initial conditions (blue), and just before first star formation (orange). At the outer edges of the disk, beyond regions of ongoing star formation, the scale height is ~ 15 pc, comparable to the scale height in the inner 200 pc prior to first star formation. Though small, both of these scale heights are resolved at our maximum resolution, 1.8 pc; we note that without feedback, our gas disk would continue to cool and collapse to an unresolved, razor thin disk. For the majority of the galaxy, stellar feedback sets the scale height. Heating, from both stellar radiation and supernovae, lifts gas above the midplane and generating scale heights between 40 and 100 pc within the half light radius. Effective galactic winds have carved out most of the gas within the inner 40 pc, distributing it somewhat smoothly above/below the midplane, leading to the significantly larger scale heights. This is made clear in the density panels if Fig 1, where regions of active star formation show a general lack of the dense, cool gas that creates the smaller scale heights at larger radii.

Interestingly, there is significant structure well above the gas disk in the form of dense clouds and filamentary features, as seen in the edge-on projections. These gas cold gas clumps appear to have typical sizes on order of ~ 10 pc, but with lower density tails that can extend up to 100 pc. These consist of both cool, self-gravitating gas clumps that are being pushed out and ablated by the stellar feedback driven winds, and gas that is cooling and condensing in the disk-halo interface of our dwarf galaxy. These clumps have typical velocities on order of a few to tens of km s $^{-1}$, and appear to survive for 10 - 100 Myr before being fully ablated or re-accreted onto the main body of the gaseous disk. The evolution of these dense clumps in the context of the disk-halo interface in our low mass dwarf galaxy will be examined in a future work. This is exciting given recent (e.g. [Zheng et al. 2017](#))

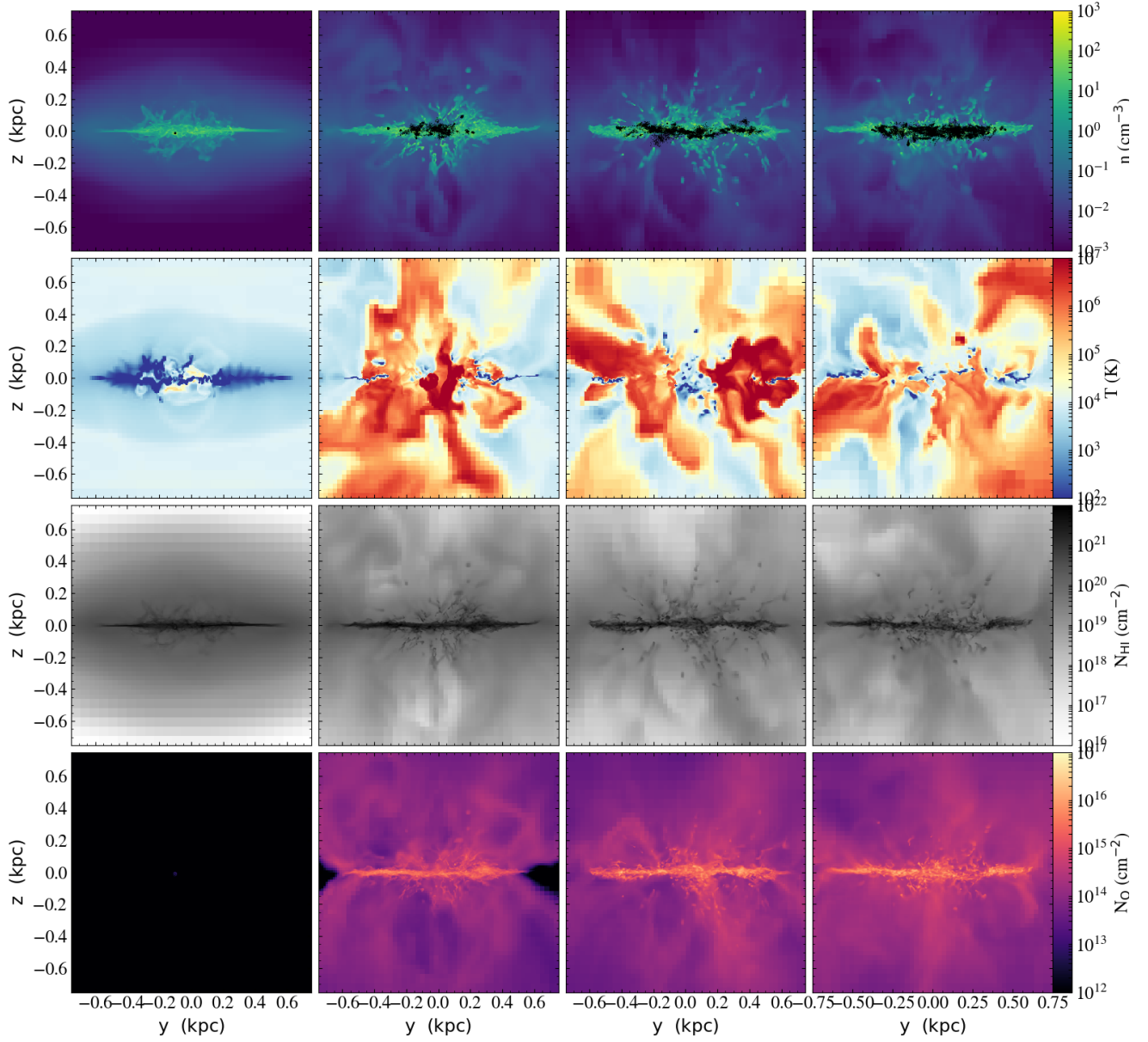


Figure 1. Draft figure - need to pretty up and finalize fields and times. Edge-on views of our dwarf galaxy at four different times in its evolution, beginning with the time at first star formation and ending at XXX Myr. Shown are density weighted projections of number density (top row), temperature slices (second row), and integrated projections giving HI column density (third row) and O column density (fourth row). Additionally, each individual main sequence star particle is shown in the number density projections as a single black dot.

and ongoing (Zheng 2017) observational work examining the disk-halo interface in nearby galaxies.

4.2. SFR and Mass Evolution

We present the star formation rate (SFR) and core collapse supernova rate (SNR) evolution of our dwarf galaxy as measured in 10 Myr bins in the left panel of Figure 4. By the end of the simulation, there have been no Type 1a supernovae.

Within the first 40 Myr of evolution the SFR rises quickly to between $2-4 \times 10^{-4} M_{\odot} \text{ yr}^{-1}$, and remains at this level with fluctuations of about a factor of 2 or less.⁹ Averaging over

⁹ The granularity in our star formation algorithm creates a lower limit in the SFR that depends on the period over which the SFR is measured (Δt). Since we produce stars in $\sim 100 M_{\odot}$ sets, the smallest value for our measured SFR is $\sim 100/\Delta t$. For $\Delta t = 10 \text{ Myr}$ this is 10^{-5} yr^{-1} . Removing the

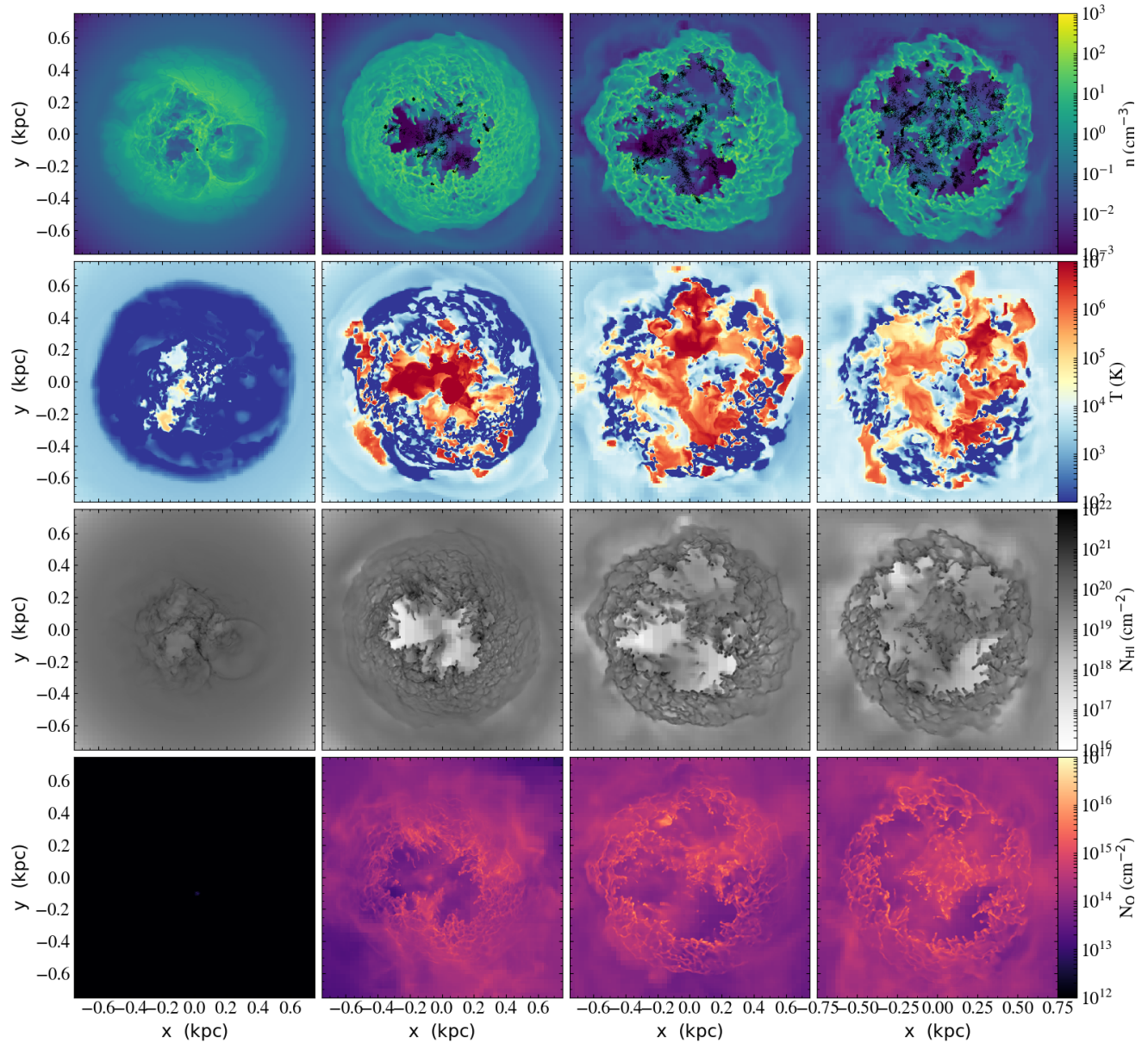


Figure 2. Draft figure - need to pretty up and finalize fields. Same as Figure 1, but showing face-on projections/slices.

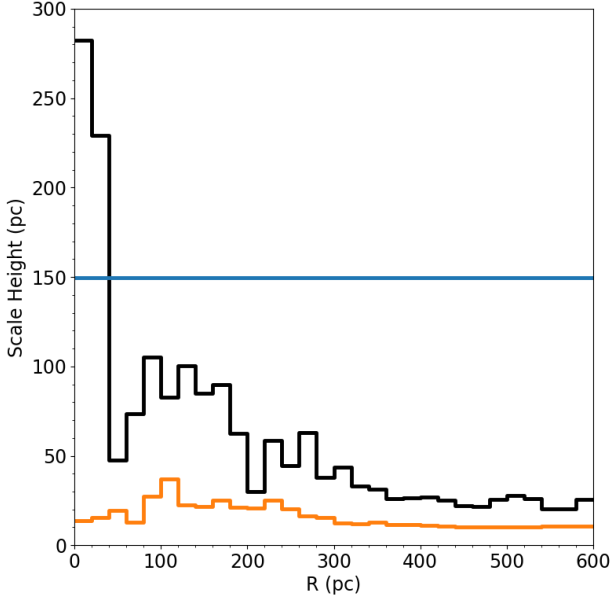


Figure 3. The average gas disk scale height as a function of radius for the last 20 Myr of simulation time (black) as compared to the uniform initial conditions (blue) and the scale height profile immediately before the first star formed (orange).

the entire simulation time since the first star was formed, we obtain a $\langle \text{SFR} \rangle = 2.34 \times 10^{-4} M_{\odot} \text{ yr}^{-1}$. The star formation rate of our model galaxy as compared to observed galaxies is discussed further in Section 5.2.

At initialization, all H and He of our dwarf galaxy is neutral, with no molecular hydrogen component. By the time of first star formation ($t = 0$ in Figure 4), HI still dominates the mass of the galaxy, but a fairly significant component of molecular hydrogen has formed, with a mass of about $6 \times 10^5 M_{\odot}$, or roughly 17% of the total mass in the galaxy's disk. The total amount of molecular hydrogen mass in the system remains fairly consistent throughout the evolution, yet its fraction increases to about 25% as the total amount of mass in the disk decreases through feedback driven winds. Small drops in the H_2 mass correspond with small increases in the total stellar mass, as some small fraction of H_2 is converted into stars, and more is destroyed from the subsequent feedback. Examining the molecular properties of the ISM in low mass dwarf galaxies in more detail is a vital avenue of future research, as there are significant observational uncertainties in deriving H_2 content of galaxies in this low metallicity

granularity requires a fundamental change in our star formation algorithm, likely at the cost of increased complexity and computational expense. Sink particles, which track pre-main sequence stellar mass accumulation, would be the most viable way to do this (see for example Krumholz et al. 2004; Federrath et al. 2010; Gong & Ostriker 2013; Bleuler & Teyssier 2014; Soriano et al. 2017).

regime (Leroy et al. 2008; McQuinn et al. 2012; Amorín et al. 2016). The molecular properties of our galaxy is discussed further in context with other works in Section 5.2.

4.3. Phase Diagrams and ISM Properties

Our simulations contain both ample resolution and micro-physics to capture a multi-phase medium within the ISM and halo of our simulated galaxy **too strong of a claim?**. We define five different gas phases following those defined in (Draine 2011): molecular, cold neutral medium (CNM), warm neutral medium (WNM), warm ionized medium (WIM), and hot ionized medium (HIM). See Appendix A for a quantitative definition of these phases. Each of these exist in our simulations, and are regulated by the complex interplay between turbulence, self-gravity, and stellar feedback throughout the galaxy's evolution. Here we discuss the phase properties of the gas throughout the simulation box and within the ISM of our dwarf galaxy.

Figure 5 shows the temperature-density phase diagram of all gas in the simulation domain, averaged over the final 50 Myr of simulation time. One can readily identify the two most massive regions of gas in the simulation, a low density, warm phase produced through ionization and supernovae heating, and a cold, high density phase which makes up most of the mass in the galaxy's disk (see Figure 6). **not completely sure what to talk about here for the diagram**

The mass of the ISM in our dwarf galaxy is dominated by the CNM over the entire simulation time, as shown in the left panel of Figure 6. Together, the CNM and WNM comprise roughly 90% of the galaxy's mass throughout most of its evolution. While the CNM has a negligible volume fraction, the WNM, WIM, and HIM occupy roughly the same volume each, though the two warm phases dominate. The volume fractions are subject to significantly more fluctuations over time, due to the low SFR and SNR of our galaxy. Together, these figures better quantify the general properties observed in the panel plots in Figure 1 and Figure 2. These results are in some contrast with those found for the more massive dwarf galaxy in Hu et al. (2016, 2017). In short, they find the mass and volume fraction of the ISM nearly entirely dominated by warm gas (ionized and neutral), with cold gas comprising $\sim 10\%$ of mass, and negligible volume, and hot gas comprising $\sim 10\%$ of the volume, but negligible mass. Our lower mass, lower metallicity galaxy contains more cold gas (by mass fraction) by a large factor, and more hot gas (by volume fraction) by a factor of a few.

4.4. Interstellar Radiation Field

The ISRF of our galaxy varies dramatically in both space and time, as has been demonstrated previously in works modelling varying radiation fields (Parravano et al. 2003; Hu et al. 2017). This is especially not surprising in the low SFR

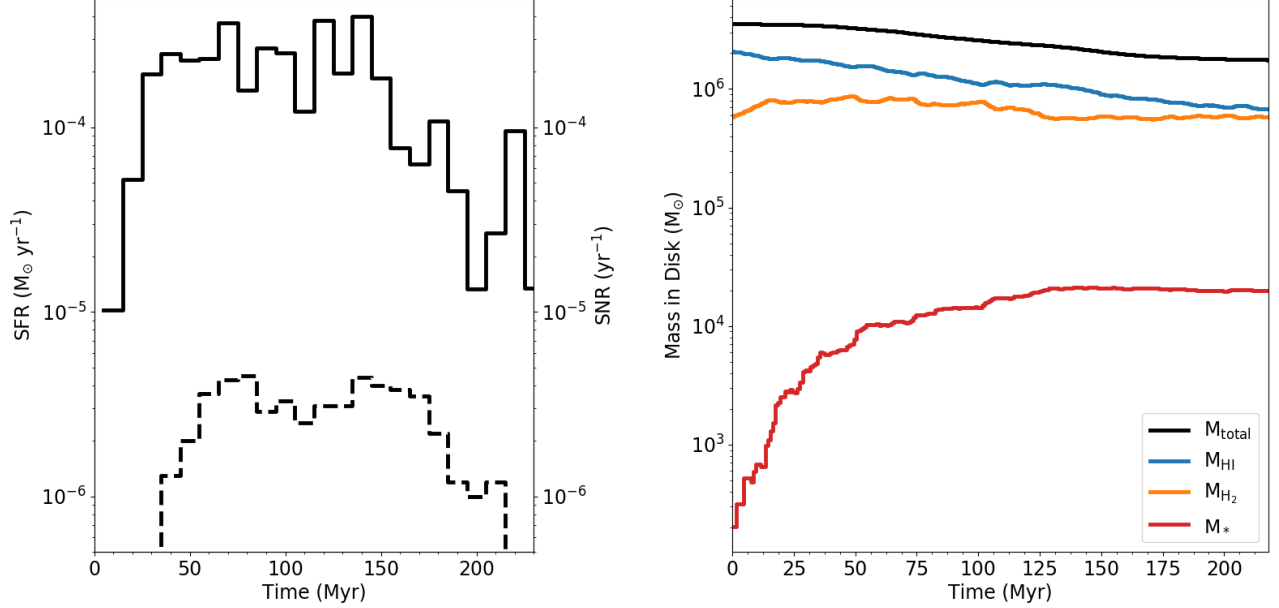


Figure 4. Left: The SFR and core collapse SNR in our dwarf galaxy in 10 Myr bins (left). Right: The evolution of the total gas mass (black), HI mass (blue), H₂ mass (orange), and stellar mass (red) in the galaxy over time. Note that the vertical axis limits in the left panel have been scaled to the same numerical values, yet with different units for the SFR and SNR.

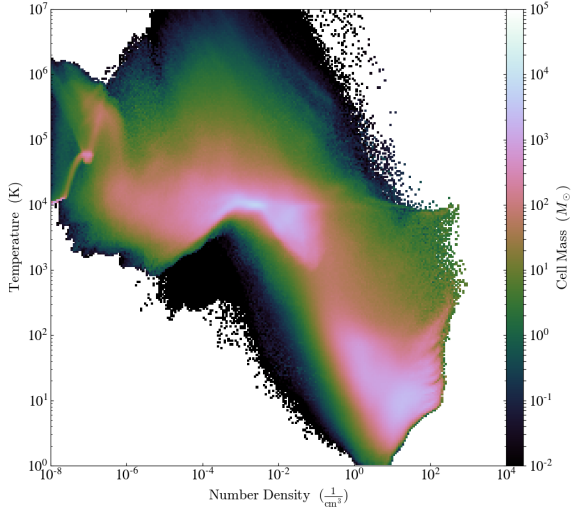


Figure 5. The full-box temperature vs. number density phase diagram of our dwarf galaxy simulation, averaged over the final 50 Myr of simulation time.

regime, where there can be large fluctuations in proximity to a massive, radiating star over time. In Figure 7 we present 1D volume averaged radial profiles of the ISRF in various bands, time averaged over the last 50 Myr of simulation time. The top panel shows the average G_o , or the ISRF flux between 6 - 13.6 eV normalized to the value in the solar neighborhood of the Milky Way (see Section XX). The contribution from the metagalactic background is below the lower vertical axis limit on this plot. The shaded region gives the minimum

and maximum value of G_o in the sampled time range. As shown, regions typically experience fluctuations in the ISRF of an order of magnitude. Interestingly, the central 200 pc does not contain the peak of the ISRF in the galaxy. This is likely a transient property, however, and is a by-product of the inside-out star formation of this dwarf galaxy. By the end of the simulation the feedback from stars produced in the central region has reduced the SFR compared to outer parts of the galaxy. The latter is thus host to more radiating young stars.

The bottom panel gives the ionizing photon fluxes (HI and HeI) from ionizing photons from the stellar radiation only. Since these fields are tracked directly with ray-tracing radiative transfer, the profiles encode information about local attenuation of these photons from dense, neutral gas. This is the main driver of the differences between these fields and G_o . In addition, we only show the average line and shade to the maximum value at any given position, since the minimum value reaches zero at all radii at some point over the 50 Myr examined. As shown, this causes the profile to vary much more dramatically at all radii. However, the same general trend is preserved of less radiation in the inner 200 pc than the region between 200 and 400 pc, and an order of magnitude or more fluctuation at all radii. The rapid drop off beyond 400 pc is due to the rapid attenuation of ionizing photons by the cold gas at large radii (see Figure 1).

These plots are useful to understand the time-varying properties of the ISRF in a spatially averaged sense. However, the local variations for individual regions can be much larger

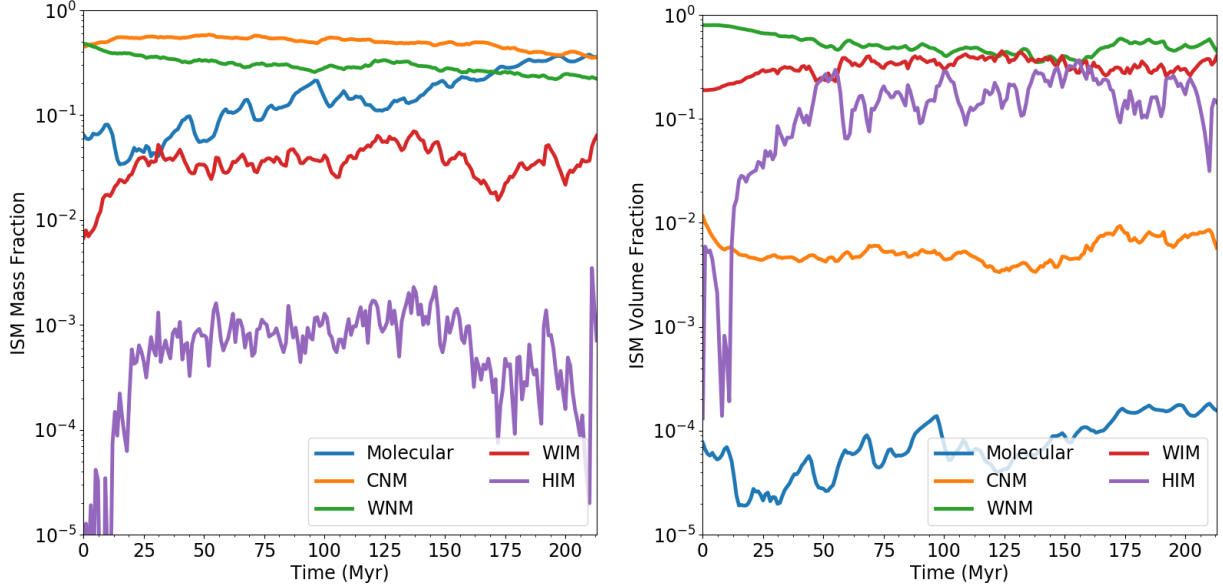


Figure 6. The evolution of the mass and volume fractions for each phase of our galaxy’s ISM. This figures only consider gas present within the disk of the galaxy.

than is illustrated in these profiles. In Figure 8 we present a 2D profile of G_o averaged over the final 50 Myr of the simulation time, which effectively captures the large spikes in local ISRF from recent star forming regions. The 1D profiles accurately capture the averaged heating / ionizing effects of the ISRF in our galaxy, which helps reduce star formation by increase the thermal pressure support and equilibrium temperature of the ISM, yet it is these spikes that act as important local feedback to shut off star formation in dense, collapsing regions that satisfy our star formation criteria. This point will be examined in more detail in future work with comparison simulations using different feedback processes (Emerick et. al. in prep).

4.5. Outflow Properties

Recent cosmological simulations of dwarf galaxies with detailed feedback over a range of dark matter halo masses find that they exhibit large outflows, with mass loading factors on order of 10 - 1000 (Muratov et al. 2015). However, comparable work of idealized dwarf galaxies with detailed feedback and physics models find more modest mass loading factors (Hu et al. 2016, 2017). In Figure 9 we present the mass outflow and mass loading rates for our dwarf galaxy as a function of time, computed at five different positions from the galaxy. We follow Muratov et al. (2015) defining the mass outflow rate (\dot{M}_{outflow}) at any given radius to be the sum of the outflow rate in all cells in a spherical annulus of width dL centered at that radius. In other words, $\dot{M}_{\text{outflow}} = \sum M_{\text{gas}} \times v_r / dL$. We choose $dL = 0.1 R_{\text{vir}}$, or 2.74 kpc.

The total mass outflow rates and mass loading factors at 0.1, 0.25, 0.5, and 1.0 R_{vir} are shown in Figure 9. We use the 10 Myr averaged SFR to compute the mass loading rates. The outflow rate at 0.1 R_{vir} is high, corresponding to mass loading factors on order of 50 - 100 throughout the simulation time. This quickly declines towards larger radii, however, with effectively zero outflow past the virial radius. Muratov et al. (2015) finds typical mass loading factors at 0.25 R_{vir} on order of 20-40 for galaxies with $v_c = 30 \text{ km s}^{-1}$ at low redshift. Our dwarf galaxy exhibits mass loading factors between 4 and 40 at this radius; this is consistent with the results from Muratov et al. (2015), but perhaps slightly below the typical values.

Interestingly, the $v_c \sim 30 \text{ km s}^{-1}$ halos examined in Muratov et al. (2015) are more massive than the $M_{\text{vir}} = 2.5 \times 10^9 M_\odot$ halo examined here by a factor of a few. Using a fit provided in Muratov et al. (2015) to extrapolate and compare at fixed halo mass, one would expect mass loading factors on order of 100 at 0.25 R_{vir} for our dwarf galaxy, a factor of a few higher than what we find. These differences could be attributed to our lack of cosmological evolution in these isolated simulations, but ultimately requires a larger set of dwarf galaxy simulations to make a more robust comparison. We note, however, that our results are much closer to the (Muratov et al. 2015) results than those in Hu et al. (2016, 2017), which find mass loading factors at 0.05 R_{vir} between 1 and 10 for a dwarf galaxy with $M_{\text{vir}} = 10^{10} M_\odot$, and therefore certainly much smaller mass loading factors at 0.25 R_{vir} .

Detailed outflow properties, beyond outflow rates and mass loading factors, are important discriminators between the model dependent feedback physics included in galaxy simu-

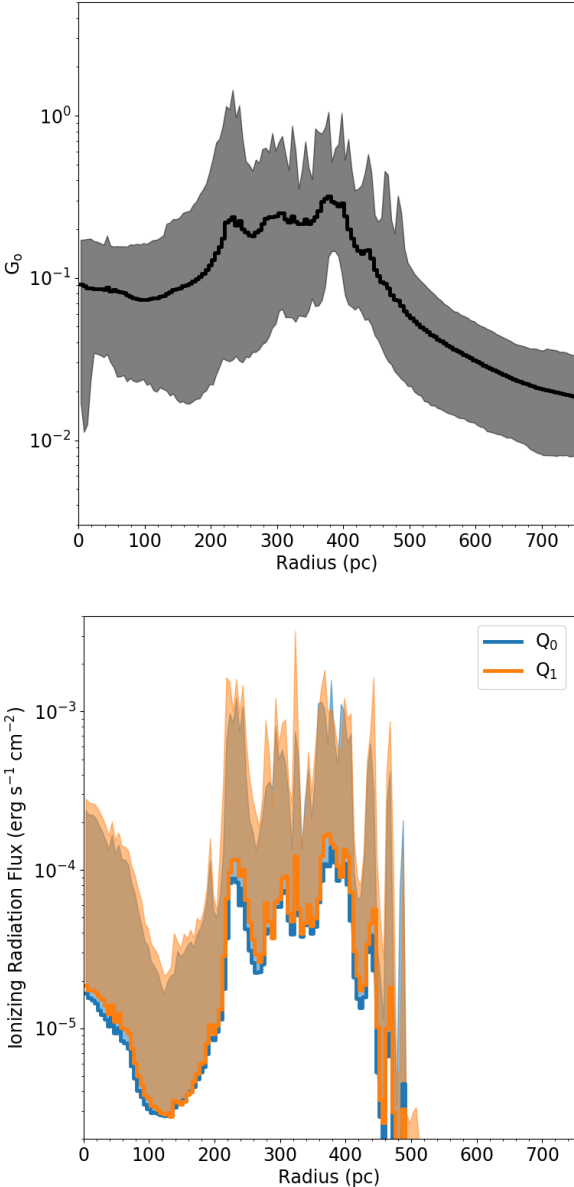


Figure 7. 1D radial profiles of the ISRF in our galaxy in three different bands, time-averaged over the final 50 Myr of simulation time. The top panel gives G_0 , or the flux of radiation between 6 - 13.6 eV normalized to the value in the solar neighborhood, shaded between minimum and maximum values at each position. The bottom panel gives the HI and HeI ionizing stellar radiation flux, showing average value and maximum values only. For these fields the minimum value reaches zero at some point over the examined period at all radii.

lations. (**do I need an example of this in recent work?**). In Figure 10 we present radial velocity distributions of all material outside our dwarf galaxy’s disk, and within the halo, broken into three gas phases. Half of the outflow, by mass, is at velocities below 40 km s^{-1} , with 75% at velocities of 70 km s^{-1} or below. This gas is dominated by the two warm

gas phases, with the WNM dominating at lower velocities, and the WIM at higher velocities. The distribution has a very long tail out to and beyond 500 km s^{-1} . The dominant launching mechanism in this simulation are supernovae (Emerick et. al. in prep), generating a rapidly moving and volume filling HIM, consistent with the results in Hu et al. (2016, 2017). However, as shown, the HIM comprises very little of the outflow by mass. Most of the outflowing gas comes from the warm phase, pushed out by the high pressure, fast moving HIM. Some of this warm gas certainly originates from adiabatically and radiatively cooled HIM, however. The amount of transfer between phases in the halo of our galaxy will be investigated in future work.

Dwarf galaxies efficiently, and preferentially, eject metals released in stellar feedback from their shallow potential wells (Mac Low & Ferrara 1999; Ferrara & Tolstoy 2000). This has been better quantified recently both observationally (e.g. Zahid et al. 2012; Peeples et al. 2014; McQuinn et al. 2015b) and with more detailed cosmological simulations (Anglés-Alcázar et al. 2017; Muratov et al. 2017). In Figure 11 we show the average ISM metallicity (black), halo metallicity (blue), and outflow metallicities (orange) at 0.1 (solid), 0.25 (dashed), and 1.0 (dotted) R_{vir} over the simulation time. The ISM metallicity evolves minimally from the initial conditions in this time, while the halo and outflow properties change significantly. It is apparent from this figure that the outflows are preferentially metal enriched, as the halo increases in metallicity by a factor of ~ 2 in the simulation time. Although most of gas mass in the halo (outside the disk) remains is within $0.2 R_{\text{vir}}$ (see Section 5.2.2), the mass that does make it out far and out side the halo is metal enriched by a factor of $\sim 5\text{-}6$ compared to the ISM. This is in contrast with the results from Muratov et al. (2017), which generally shows $Z_{\text{outflow}} \simeq Z_{\text{ISM}}$ at $0.25 R_{\text{vir}}$ and $Z_{\text{outflow}} < Z_{\text{ISM}}$ at $1.0 R_{\text{vir}}$, though both with some scatter that reaches above $Z_{\text{outflow}} > Z_{\text{ISM}}$, especially at high redshift. However, we note that our simulations certainly do not contain a cosmologically realistic CGM and do not include ongoing cosmological accretion of pristine gas; this will certainly lower the typical halo and outflow metallicities, possibly more in agreement with the findings of Muratov et al. (2017).

4.6. Chemical Evolution

Observations of Local Group dwarf galaxies have shown that they retain very little of the total amount of metals they are expected to have produced, given their star formation histories (see Section 5.2). In Figure 12 we show the fraction of metals retained within the disk / expelled into the halo of our galaxy over time, along with a break down of the locations of each metal species by the end of the simulation time. As shown in the top panel, a majority of each metal tracer species is found outside the disk of the galaxy, in the galaxy

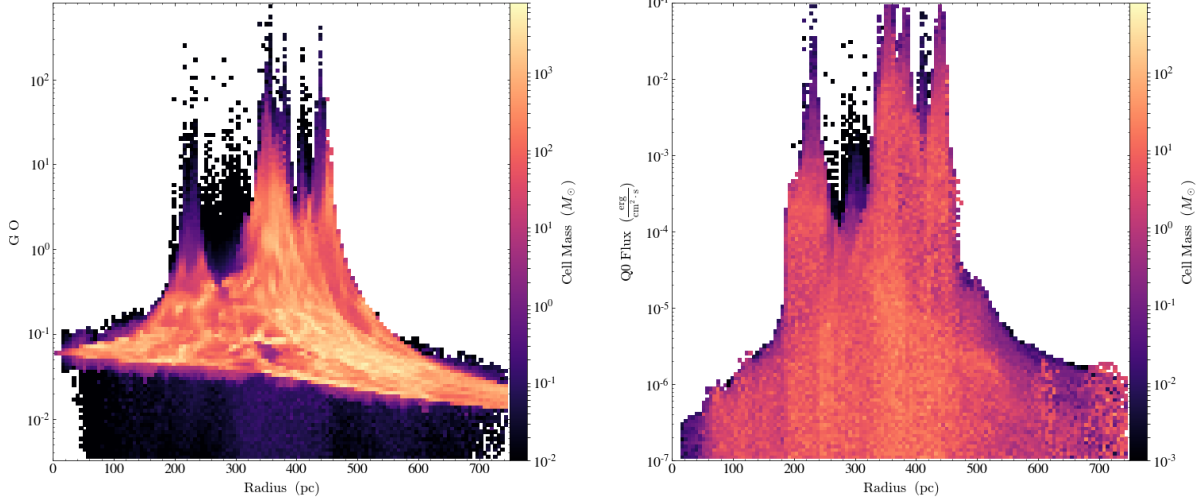


Figure 8. Single-snapshot 2D radial profile plots of the ISRF in two flux bands, G_0 and HI ionizing radiation, illustrating the full dynamic range of radiation flux at a given radius in the galaxy. Here, we include all gas within 25 pc of the midplane of our dwarf galaxy. We note the large difference in color scale between the two plots. Since a majority of the mass of the galaxy is in the cold phase (see Figure 5), and is therefore optically thick to HI ionizing radiation, it does not show up in the HI ionizing radiation diagram. This gas readily appears in the G_0 since we assume it to be optically thin, though do apply a localized shielding approximation.

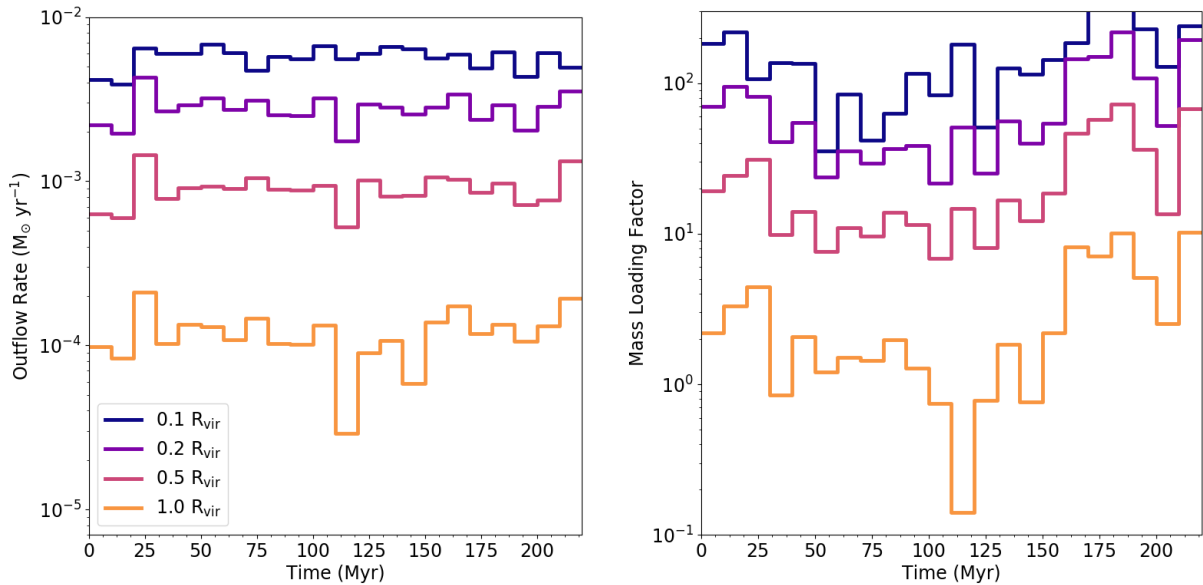


Figure 9. Spherical mass outflow rates and mass loading rates over time at 4 different radii from the galaxy.

halo. In total, **85%** of the tracer metal species produced lie outside of the disk of our galaxy. Interestingly, the exact fraction is not uniform across metal species. Most notably, Nitrogen, is preferentially retained by the galaxy over the other species.

Roughly **35%** of the N produced remains in the disk, as compared to **15%** of O and **15%** of Fe, for example. This difference is entirely feedback driven, but a coincidence of our particular galaxy conditions. At our galaxy's metallicity, the IMF weighted production of N rests entirely with the

stellar winds of stars between 8 and $10 M_\odot$; there is little to no N production in supernovae at this metallicity. The rest of the species either have very little stellar wind production, produced solely in supernovae, or have similar production levels between both supernovae and stellar winds (like O, for example). The typically lower injection energies of N into the galaxy than the SN injected elements means N is preferentially retained within the ISM, and not as effectively ejected through outflows. In truth, the stars that produce N do eventually explode as supernovae, sweeping up some frac-

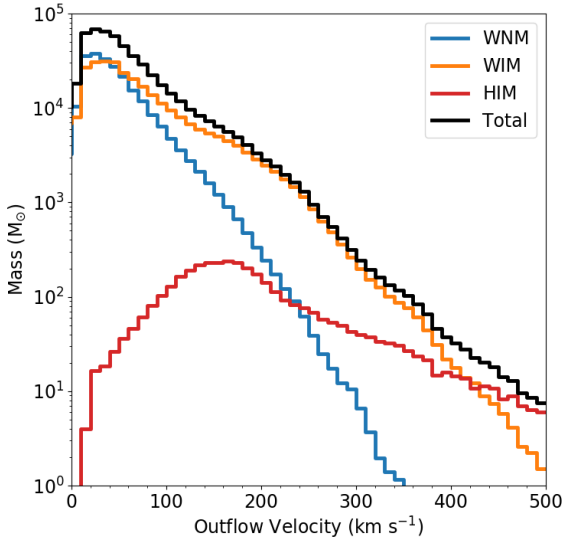


Figure 10. The time averaged radial velocity distribution of outflowing material external to the disk and within the virial radius of our dwarf galaxy. The outflowing material is multiphase, broken into WNM, WIM, and HIM. See XXX for definitions of these regimes. We note that WNM is often labeled simply as “cold”, or gas below $T = 10^4$ K. There is little to no outflowing mass in the CNM or molecular phases.

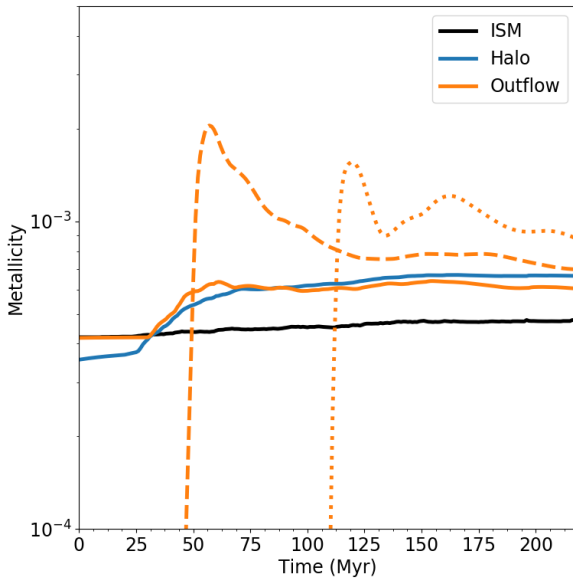


Figure 11. The mass-weighted average metallicity of our dwarf galaxy’s ISM, halo, and outflowing gas at 0.1 (solid), 0.25 (dashed), and 1.0 (dotted) R_{vir} over the simulation time. The halo is defined as the region outside of the disk, yet inside the virial radius.

tion of the wind produced N into outflows. However, clearly some of this N is able to mix more effectively within the ISM than the other metal species. How abundance variations like this evolve over longer timescales and with varying feedback physics is the subject of ongoing work (Emerick et. al. in prep.).

The bottom panel illustrates where these metals are partitioned within the ISM of the galaxy at the end of the simulation time. The CNM contains roughly 50-60% of each species, with the CNM and WNM together accounting for most of the metals in the galaxy. The WIM contains only $\sim 10\%$ of each species, with the HIM containing very little. This may be counterintuitive to the fact that most metals are initially injected into the galaxy in either the WIM or HIM phases. However, the disk metals represent only a small fraction of the total metals produced. Much of the metals are effectively removed from the disk into the halo (see Section 4.5). It is apparent that the remaining metals quickly mix or cool into denser gas phases.

4.7. Stellar Abundances

This section needs work. As per discussion with Keith and Kathryn, displaying abundance evolution like this is confusing and misleading. Switch to discussion of mass / abundance fraction evolution of individual specie(s). We plot the $[\alpha/\text{Fe}] - [\text{Fe}/\text{H}]$ ratio for all star particles in our simulation that are “alive” in Figure 13. This represents stars that have not gone supernovae or have otherwise formed a compact object. Here, $\alpha = (\text{O} + \text{Mg} + \text{Si})/3.0$, and the notation $[\text{X}/\text{Y}]$ denotes the ratio of the abundance of species X over Y, relative to the solar value, or $\log([\text{X}/\text{Y}]) = \log(\text{X}/\text{Y}) - \log(\text{X}_\odot/\text{Y}_\odot)$. All stars are colored by their age.

As expected, there is a noticeable trend of stellar age with $[\text{Fe}/\text{H}]$; especially in our case as the overall iron abundance is gradually increasing, yet we do not have any accretion of primordial material. Interestingly, the few stars with the highest $[\text{Fe}/\text{H}]$, between -3 and -2, are not the most recently formed; the most recent star formation is clustered around $[\text{Fe}/\text{H}]$ between -3 and -4.

We note the “knee” like feature at very low $[\text{Fe}/\text{H}]$ is not the characteristic knee seen in $[\alpha/\text{Fe}] - [\text{Fe}/\text{H}]$ space, corresponding to the period when iron enrichment from SNIa begins to make a significant contribution to the galactic chemical evolution. This generally occurs after roughly 1 Gyr of stellar evolution, far longer than the 170 Myr simulated here.

5. DISCUSSION

5.1. Comparison to Previous Work

At the moment, doing a lot of this throughout paper. Not certain if I need an explicit, separate discussion here.

5.2. Comparison to Observed Low Mass Dwarf Galaxies

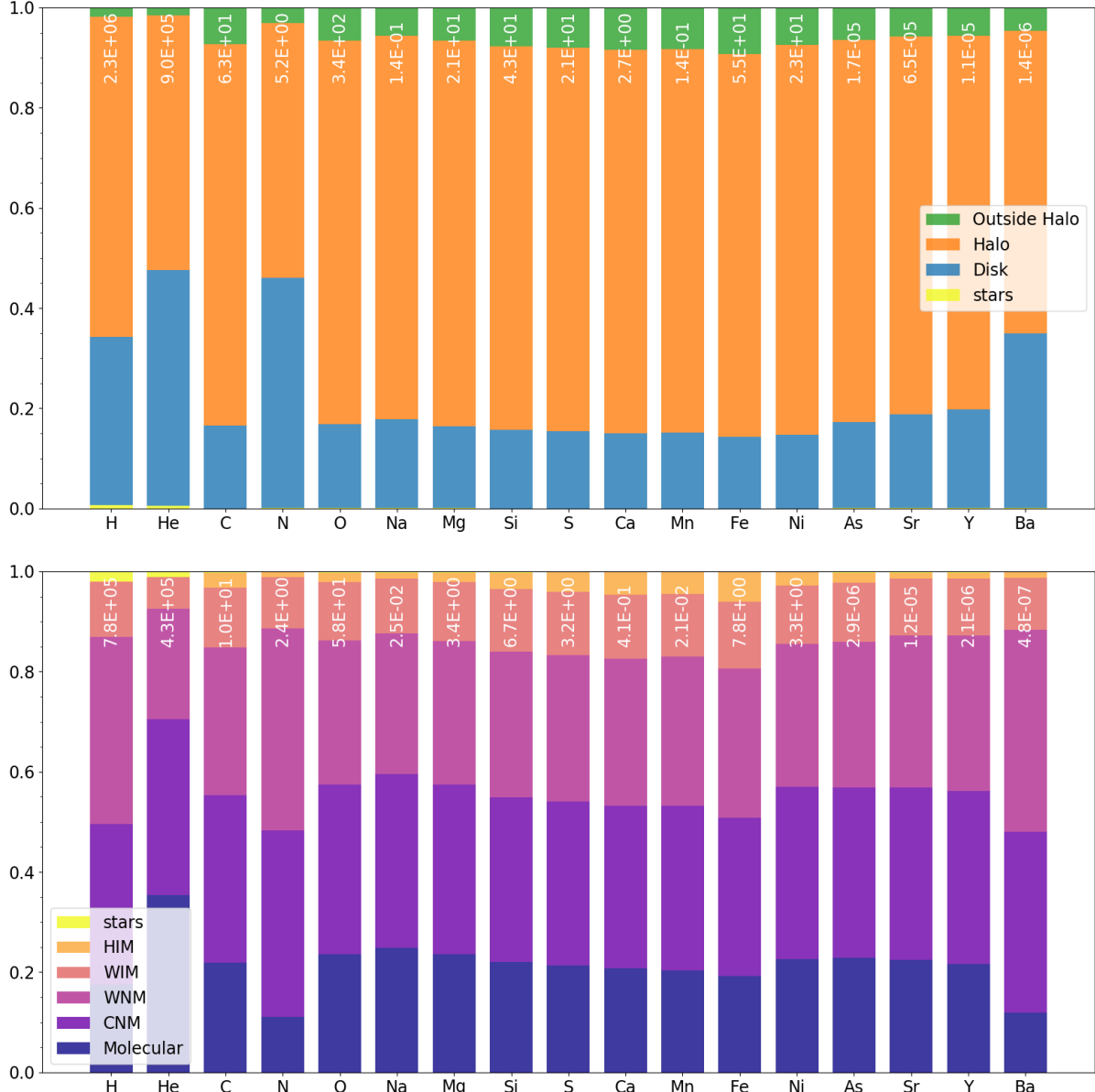


Figure 12. The fraction of each species in the full simulation box contained in the halo, gas in the galaxy disk, and stars (top), and the fraction of species within the disk alone each in phase of the ISM (bottom).

5.2.1. Gas and Star Formation

The observational sample of isolated, gaseous, low mass dwarf galaxies is limited compared to more massive galaxies, but has improved substantially with recent blind and targeted HI surveys (e.g. Giovanelli et al. 2005; Geha et al. 2006, 2012; Walter et al. 2008; Cannon et al. 2011; Haynes et al. 2011; Hunter et al. 2012; Bradford et al. 2015; Tollerud et al. 2015; Sand et al. 2015). However, the sample of isolated dwarf galaxies with $M_* < 10^7 M_\odot$ remains small. In Figure 14 we show where our galaxy lies relative to the observed Kennicutt-Schmidt (KS) law (left) for low mass galaxies, and the extended Schmidt law (ESL) (right) which has

been shown recently to be extend to low mass, low metallicity dwarf galaxies (Roychowdhury et al. 2017). We plot our galaxy every 1 Myr in these diagrams, showing the significant temporal variation in both spaces. Although these quantities are conceptually simple, due to how these values are measured observationally it is challenging to make a direct comparison to simulations, particularly in defining the geometric region to measure the surface densities. We have attempted to make a reasonable analog to how Σ_{sfr} and Σ_{gas} are measured observationally for low mass dwarfs following what is described in Roychowdhury et al. (2014). We define $\Sigma_{\text{sfr}} = \dot{M}_{*,10\text{Myr}}/A_{*,10\text{Myr}}$, where $\dot{M}_{*,10\text{Myr}}$ is the SFR measured

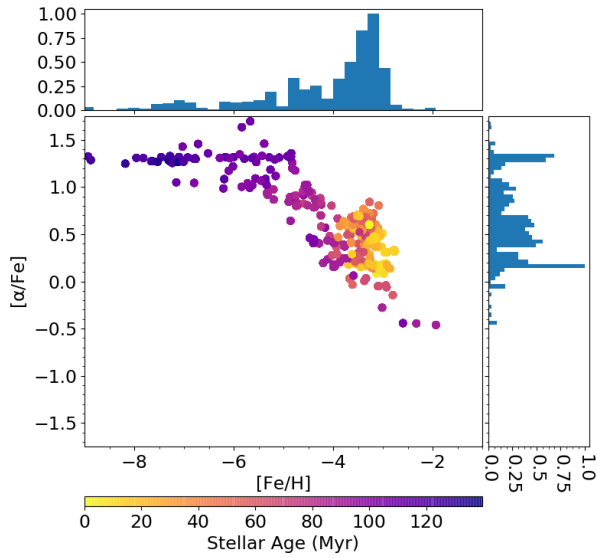


Figure 13. The $[\alpha/\text{Fe}] - [\text{Fe}/\text{H}]$ diagram for all stars in our simulation, colored by their age. Here, we define $\alpha = (\text{O} + \text{Mg} + \text{Si})/3.0$. Each histogram shows counts, normalized to the peak in each distribution.

over the preceding 10 Myr, and $A_{*,10\text{Myr}}$ is the disk defined out to the farthest star formed within the previous 10 Myr. Likewise, $\Sigma_{\text{gas}} = M_{\text{gas},10\text{Myr}}/A_{*,10\text{Myr}}$, where $M_{\text{gas},10\text{Myr}}$ is the total gas mass within this defined disk. However, the total gas content cannot be determined observationally, particularly for low mass dwarf galaxies with a virtually unmeasurable H_2 content. Therefore, we present Σ_{gas} as measured directly in the simulations (green/purple points) and the observational equivalent, or $\Sigma_{\text{gas,obs}} = 1.34 \times \Sigma_{\text{HI}}$, where the factor 1.34 attempts to account for He, and where there is no correction for H_2 (plasma points).

In both panels, we also include recent observational constraints from these relationships. We include the KS fits from Shi et al. (2011) with 1σ errors (black), the fits from Roychowdhury et al. (2014) (blue), and the individual points from the recent SHIELD sample (Teich et al. 2016); we include only the fit and 1σ errors from (Shi et al. 2011) for the ESL (black), which have been shown to match well for dwarf galaxies at these surface densities (Roychowdhury et al. 2017). In both relationships our simulations fit well around the median observed fit, spanning the 1σ variations about the mean. This is a remarkable result. In constructing our galaxy model, we employed *no* tuning of the underlying physics, adopting only canonical values for any available free parameters. It is non-trivial that our galaxy should oscillate about the median relationships in Fig. 14, but signifies a proper accounting of the relevant physics governing gas and star forming properties in our galaxy. This result is consistent with recent galactic evolution simulations run at high resolution.

tion with a detailed accounting of stellar feedback physics (*relevant citations*)

The molecular gas content of low mass dwarf galaxies like this is generally considered to be small, (references). Assuming the relationship in Leroy et al. (2013) and Momose et al. (2013), Roychowdhury et al. (2014) finds typical molecular gas fractions anywhere from $f_{\text{H}_2} = 0.05$ to $f_{\text{H}_2} = 0.5$; a significant range in values. Given As discussed in Section 2.4, our galaxy has f_{H_2} typically of 0.17 - 0.20, in between this range, but significantly above the few percent often found in models. This means ignoring the H_2 component of our galaxies leads to an average shift of 0.24 dex to the right in the KS relationship, and 0.24 dex right and down in the ESL. This does not lead to a significant disagreement with the observed relationships, but would constitute a quantitative change to the observed fits if our f_{H_2} is robust for low mass, low metallicity dwarf galaxies. However, our non-equilibrium chemical model for H_2 formation and destruction is relatively simple, and does not account for C and O chemistry, a detailed dust model, or cosmic rays; all of which may significantly affect f_{H_2} . Simulations in Hu et al. (2016) and Hu et al. (2017), which contain a more detailed non-equilibrium chemistry model than included here, give very low f_{H_2} , below 10^{-4} for their full feedback simulations; even their simulations without any radiation feedback only reach $f_{\text{H}_2} \sim 2 \times 10^{-3}$. However, their simulated dwarf galaxies are more massive ($M_{\text{vir}} = 10^{10} M_{\odot}$) and higher metallicity ($Z = 0.1 Z_{\odot}$) than those examined here. This disagreement warrants additional investigation, particularly as making predictions for the H_2 content of low mass dwarf galaxies is valuable. We do note that there is some possible observational evidence for higher than expected ($\sim 15\%$) molecular fractions (Schruba et al. 2017), though this still remains highly uncertain.

5.2.2. Metal Retention

Unfortunately, these high resolution simulations are not (yet) run for the $\sim \text{Gyr}$ timescales required to make direct comparisons to the observed stellar and gas phase metallicities of comparable dwarf galaxies at $z = 0$. However, we can compare to a key observable, the ejection / retention fraction of metals within stars and the galaxy's ISM compared to what would be expected from stellar evolution models based on the galaxy's star formation history. This can be done readily with Milky Way dSph's, whose stars seem to retain very little of the expected metals produced, on order of a few percent or less depending on the galaxy and the species (Kirby et al. 2011). However, environmental effects, namely ram pressure and tidal stripping, complicate the understanding of how these metals were removed from the galaxy. Leo P, the dwarf galaxy we approximate in our initial conditions, is extremely valuable as a gaseous, star forming low mass dwarf

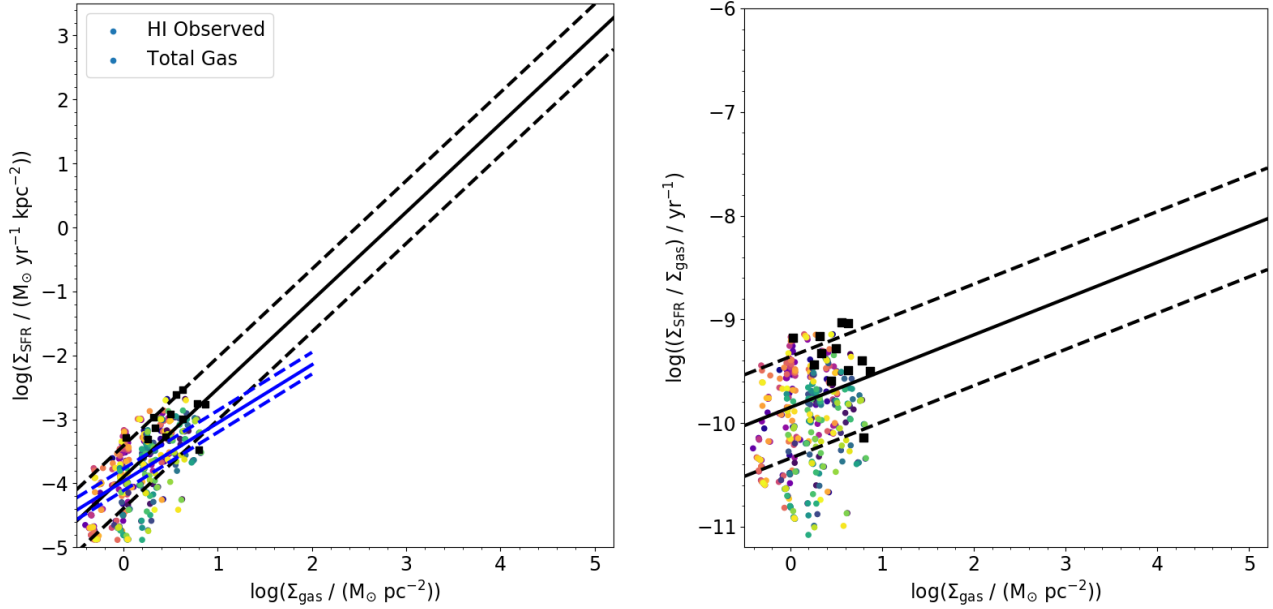


Figure 14. The KS law (left) and ESL (right) relationships for our galaxy as measured every 1 Myr for the total gas surface density computed from the simulations, and an observational analog derived using the HI content (see text for details).

galaxy close enough to the Milky Way to conduct this experiment and with an observable HII region, necessary for determining gas phase abundances. Leo P retains $\sim 5\% \pm 2\%$ of its metals, $\sim 1\%$ in stars and the rest in ISM gas (McQuinn et al. 2015b). As discussed in Section 4.6, roughly 95% of the tracked metals produced throughout the simulation time no longer reside within the galaxy’s disk. At the end of our simulation, we agree with the observations; however, this is an evolving quantity that also depends on how much (if any) subsequent re-accretion of these metals occurs. Although more than half of these metals are expected to be re-accreted (Anglés-Alcázar et al. 2017), it is still possible that, at any moment, most of the metals that have been produced lie outside the galaxy disk. We will examine the long term, and species-by-species, evolution of the metal retention fraction in future work.

It is interesting to consider where these metals lie outside of the galaxy’s disk, in the CGM or ejected into the IGM, and their eventual fate. While this cannot be observationally determined for dwarf galaxies at this mass, cosmological simulations of a $M_{\text{vir}} = 10^{10} \text{ M}_\odot$ galaxy show that, by redshift zero $\sim 60\%$ of ejected gas is recycled over time, while 40% is ejected from the galaxy’s halo (Anglés-Alcázar et al. 2017). In our case, no metals have been ejected outside the virial radius; this is possibly not surprising however given that metals ejected outside the halo would need to travel with an average velocity of 150 km s^{-1} for the entirety of our simulation time. 32% of all metals lie within 1 kpc of the center of our galaxy, 75% within $0.25 R_{\text{vir}}$ (or 6.85 kpc), and only 10% outside R_{vir} . Over time, the re-accretion or final ejec-

tion of this gas is directly relevant to the chemical evolution of low mass dwarf galaxies. Re-cycling of metal enriched gas, could be a significant source of long-term chemical evolution in low mass galaxies, particularly if a majority of metals ejected from the disk (itself nearly all the metals produced by the galaxy) returns. Unfortunately, we cannot yet speak to how this gas evolves over time, but will investigate this in future work with our feedback model.

5.3. Missing Physics

Although we include detailed physics in our simulations, there remains additional physics that may be relevant. These are discussed below.

5.3.1. Full Stellar Wind Model

As discussed previously, our stellar wind model significantly reduces the injected wind velocity from $\sim 1000 \text{ km s}^{-1}$ to 1 km s^{-1} . Although our model is capable of generating realistic stellar winds with temperature profiles and radial evolution comparable to those expected from analytic calculations (Weaver et al. 1977), the hot, fast winds place a near constant and severe constraint on the Courant time step that renders $\gtrsim 100$ Myr simulations impractical. When considered in isolation, stellar winds are an important source of pre-SN feedback and do dramatically influence the dynamical evolution on molecular cloud and galaxy scales (Dale & Bonnell 2008; Peters et al. 2017; Gatto et al. 2017). However, when considered together with ionizing radiation, stellar winds contain less total energy (Agertz et al. 2013) and do not seem to have a significant dynamical influence in either idealized simulations (Geen et al. 2015) or GMCs (Dale

et al. 2014). They are even less relevant in the low-metallicity regime studied here, as stellar winds become weaker with decreasing metallicity (Puls et al. 2000; Vink & de Koter 2005). Although they likely have minimal dynamical importance, a full model of stellar winds may affect detailed ISM properties and metal mixing, warranting a closer examination in a future work.

5.3.2. Cosmic Rays and Magnetic Fields

Recent work has explored the importance of cosmic ray feedback in regulating the ISM and wind properties in galactic disks (Hanasz et al. 2013; Girichidis et al. 2016; Simpson et al. 2016; Farber et al. 2017) and simulations of both isolated (Salem et al. 2016, 2015; Pakmor et al. 2016; Ruszkowski et al. 2017) and cosmological galaxies (Salem et al. 2014). These relativistic charged particles act as a source of non-thermal pressure support in the galaxy’s ISM, capable of driving outflows with different phases and velocities than those driven through stellar feedback alone (Salem et al. 2016). Modeling cosmic rays is challenging, however, as they encompass a wide range of energies (give range), with significant uncertainties in how they propagate through the ISM (e.g. Wiener et al. 2017). Their propagation is often modeled as a diffusive process, but in truth this diffusion should vary depending on cosmic ray energy. In addition, cosmic rays couple effectively to the magnetic fields of galaxies, diffusing preferentially along structured magnetic field lines within the ISM. Modeling cosmic ray feedback completely requires both an accurate cosmic ray model and magnetohydrodynamics in order to capture the interplay of these two physical phenomena. Finally, including MHD presents additional difficulties in untangling the effects each individual feedback mechanism on galaxy chemodynamics.

We do note that an isotropic, two-fluid model for cosmic ray feedback exists in ENZO (Salem & Bryan 2014; Salem et al. 2015) and has been well tested. Mechanically, including cosmic ray feedback in our model is trivial. However, the cosmic ray population, their diffusion coefficient, and the magnetic field structure of the lowest mass dwarf galaxies each have significant enough uncertainties to warrant reserving their full inclusion into our model to a later work.

5.4. Detailed Dust Model

Should we discuss this? If so I definitely need more info and references - AE. The dust content of our galaxy is modeled only approximately, scaling with the cell-to-cell variations in gas metallicity. Explicitly following the dust content in our galaxy, even crudely, could introduce significant variations in local cooling and heating rates. Accounting for metals trapped in a dust phase would produce additional variations in the cooling rates and potentially changes to the galactic chemodynamical evolution.

5.5. Detailed Stellar Evolution and Binary Stars

Definitely a question that comes up a lot whenever I say our simulations are star-by-star and detailed (as in “but what about binary stars”?). Do we need to discuss this here as a quick paragraph about how it would affect feedback properties (namely radiation and different stellar lifetimes)? (Ma et al. 2016b)

6. CONCLUSION

You can ignore this for now, I’m saving it after the first iteration (AE) We present a new method for simulating the evolution of low mass galaxies with detailed feedback and chemical enrichment as traced through individual star particles. This model follows multi-channel stellar feedback in detail, accounting for stellar winds, core collapse and Type Ia supernovae, ionizing radiation followed through radiative transfer, photoelectric heating, and LW radiation. This is in addition to the detailed cooling, heating, and chemistry followed through Grackle, including a self-consistent model for gas self-shielding from the metagalactic UVB.

In this work, we presented the initial results of these methods applied to the evolution of an isolated, low mass dwarf galaxy modeled after the $z = 0$ properties of the Leo P ultra-faint dwarf galaxy.

In future works we will investigate in detail the role each individual feedback process has in governing the chemodynamical evolution of isolated, low mass dwarf galaxies. These simulations will demonstrate how feedback affects metal mixing within the ISM and the enrichment of future stellar populations, in addition to how feedback influence metal ejection into, and possibly beyond, the galaxy’s dark matter halo. **will finish at very end**

REFERENCES

- Agertz, O., & Kravtsov, A. V. 2015, *ApJ*, 804, 18
 Agertz, O., Kravtsov, A. V., Leitner, S. N., & Gnedin, N. Y. 2013, *ApJ*, 770, 25
 Agertz, O., Moore, B., Stadel, J., et al. 2007, *MNRAS*, 380, 963
 Amorín, R., Muñoz-Tuñón, C., Aguerri, J. A. L., & Planesas, P. 2016, *A&A*, 588, A23
 Anglés-Alcázar, D., Faucher-Giguère, C.-A., Kereš, D., et al. 2017, *MNRAS*, 470, 4698
 Asplund, M., Grevesse, N., Sauval, A. J., & Scott, P. 2009, *ARA&A*, 47, 481
 Aubert, D., Deparis, N., & Ocvirk, P. 2015, *MNRAS*, 454, 1012

- Baczynski, C., Glover, S. C. O., & Klessen, R. S. 2015, *MNRAS*, **454**, 380
- Bakes, E. L. O., & Tielens, A. G. G. M. 1994, *ApJ*, **427**, 822
- Bergin, E. A., Hartmann, L. W., Raymond, J. C., & Ballesteros-Paredes, J. 2004, *ApJ*, **612**, 921
- Bleuler, A., & Teyssier, R. 2014, *MNRAS*, **445**, 4015
- Boylan-Kolchin, M., Bullock, J. S., & Kaplinghat, M. 2011, *MNRAS*, **415**, L40
- . 2012, *MNRAS*, **422**, 1203
- Bradford, J. D., Geha, M. C., & Blanton, M. R. 2015, *ApJ*, **809**, 146
- Bressan, A., Marigo, P., Girardi, L., et al. 2012, *MNRAS*, **427**, 127
- Brook, C. B., Stinson, G., Gibson, B. K., et al. 2014, *MNRAS*, **443**, 3809
- Bryan, G. L., Norman, M. L., Stone, J. M., Cen, R., & Ostriker, J. P. 1995, *Computer Physics Communications*, **89**, 149
- Burkert, A. 1995, *ApJL*, **447**, L25
- Cannon, J. M., Giovanelli, R., Haynes, M. P., et al. 2011, *ApJL*, **739**, L22
- Ceverino, D., Klypin, A., Klimek, E. S., et al. 2014, *MNRAS*, **442**, 1545
- Cohen, J. G., Christlieb, N., Thompson, I., et al. 2013, *ApJ*, **778**, 56
- Colella, P., & Woodward, P. R. 1984, *Journal of Computational Physics*, **54**, 174
- Côté, B., Ritter, C., O’Shea, B. W., et al. 2016a, *ApJ*, **824**, 82
- Côté, B., Silvia, D., O’Shea, B. W., Smith, B., & Wise, J. H. 2017, ArXiv e-prints, [arXiv:1710.06442](https://arxiv.org/abs/1710.06442)
- Côté, B., West, C., Heger, A., et al. 2016b, *MNRAS*, **463**, 3755
- Dale, J. E., & Bonnell, I. A. 2008, *MNRAS*, **391**, 2
- Dale, J. E., Ercolano, B., & Bonnell, I. A. 2012, *MNRAS*, **424**, 377
- Dale, J. E., Ngoumou, J., Ercolano, B., & Bonnell, I. A. 2014, *MNRAS*, **442**, 694
- Davé, R., Rafieferantsoa, M. H., Thompson, R. J., & Hopkins, P. F. 2017, *MNRAS*, **467**, 115
- De Silva, G. M., Freeman, K. C., Bland-Hawthorn, J., et al. 2015, *MNRAS*, **449**, 2604
- Draine, B. T. 2011, Physics of the Interstellar and Intergalactic Medium
- Escala, I., Wetzel, A., Kirby, E. N., et al. 2017, ArXiv e-prints, [arXiv:1710.06533](https://arxiv.org/abs/1710.06533)
- Farber, R., Ruszkowski, M., Yang, H.-Y. K., & Zweibel, E. G. 2017, ArXiv e-prints, [arXiv:1707.04579 \[astro-ph.HE\]](https://arxiv.org/abs/1707.04579)
- Federrath, C., Banerjee, R., Clark, P. C., & Klessen, R. S. 2010, *ApJ*, **713**, 269
- Ferrara, A., & Tolstoy, E. 2000, *MNRAS*, **313**, 291
- Ferrero, I., Abadi, M. G., Navarro, J. F., Sales, L. V., & Gurovich, S. 2012, *MNRAS*, **425**, 2817
- Few, C. G., Courty, S., Gibson, B. K., et al. 2012, *MNRAS*, **424**, L11
- Few, C. G., Courty, S., Gibson, B. K., Michel-Dansac, L., & Calura, F. 2014, *MNRAS*, **444**, 3845
- Forbes, J. C., Krumholz, M. R., Goldbaum, N. J., & Dekel, A. 2016, *Nature*, **535**, 523
- Frebel, A., & Norris, J. E. 2015, *ARA&A*, **53**, 631
- Fryer, C. L., Belczynski, K., Wiktorowicz, G., et al. 2012, *ApJ*, **749**, 91
- Garrison-Kimmel, S., Boylan-Kolchin, M., Bullock, J. S., & Kirby, E. N. 2014, *MNRAS*, **444**, 222
- Gatto, A., Walch, S., Naab, T., et al. 2017, *MNRAS*, **466**, 1903
- Geen, S., Rosdahl, J., Blaizot, J., Devriendt, J., & Slyz, A. 2015, *MNRAS*, **448**, 3248
- Geha, M., Blanton, M. R., Masjedi, M., & West, A. A. 2006, *ApJ*, **653**, 240
- Geha, M., Blanton, M. R., Yan, R., & Tinker, J. L. 2012, *ApJ*, **757**, 85
- Genel, S., Vogelsberger, M., Springel, V., et al. 2014, *MNRAS*, **445**, 175
- Gilmore, G., Randich, S., Asplund, M., et al. 2012, *The Messenger*, **147**, 25
- Giovanelli, R., Haynes, M. P., Kent, B. R., et al. 2005, *AJ*, **130**, 2598
- Giovanelli, R., Haynes, M. P., Adams, E. A. K., et al. 2013, *AJ*, **146**, 15
- Girichidis, P., Naab, T., Walch, S., et al. 2016, *ApJL*, **816**, L19
- Glover, S. C. O., & Abel, T. 2008, *MNRAS*, **388**, 1627
- Goldbaum, N. J., Krumholz, M. R., & Forbes, J. C. 2015, *ApJ*, **814**, 131
- . 2016, *ApJ*, **827**, 28
- Gong, H., & Ostriker, E. C. 2013, *ApJS*, **204**, 8
- Graur, O., & Maoz, D. 2013, *MNRAS*, **430**, 1746
- Guedes, J., Callegari, S., Madau, P., & Mayer, L. 2011, *ApJ*, **742**, 76
- Haardt, F., & Madau, P. 2012, *ApJ*, **746**, 125
- Habing, H. J. 1968, *BAN*, **19**, 421
- Hanasz, M., Lesch, H., Naab, T., et al. 2013, *ApJL*, **777**, L38
- Haynes, M. P., Giovanelli, R., Martin, A. M., et al. 2011, *AJ*, **142**, 170
- Heger, A., Fryer, C. L., Woosley, S. E., Langer, N., & Hartmann, D. H. 2003, *ApJ*, **591**, 288
- Hirai, Y., & Saitoh, T. R. 2017, *ApJL*, **838**, L23
- Hopkins, P. F., Kereš, D., Oñorbe, J., et al. 2014, *MNRAS*, **445**, 581
- Hopkins, P. F., Quataert, E., & Murray, N. 2012, *MNRAS*, **421**, 3488
- Hopkins, P. F., Wetzel, A., Keres, D., et al. 2017, ArXiv e-prints, [arXiv:1702.06148](https://arxiv.org/abs/1702.06148)
- Hu, C.-Y., Naab, T., Glover, S. C. O., Walch, S., & Clark, P. C. 2017, ArXiv e-prints, [arXiv:1701.08779](https://arxiv.org/abs/1701.08779)

- Hu, C.-Y., Naab, T., Walch, S., Glover, S. C. O., & Clark, P. C. 2016, *MNRAS*, **458**, 3528
- Hunter, D. A., Ficut-Vicas, D., Ashley, T., et al. 2012, *AJ*, **144**, 134
- Jeon, M., Besla, G., & Bromm, V. 2017, *ApJ*, **848**, 85
- Kawata, D., & Gibson, B. K. 2003, *MNRAS*, **346**, 135
- Kim, J.-h., Krumholz, M. R., Wise, J. H., et al. 2013a, *ApJ*, **775**, 109
- . 2013b, *ApJ*, **779**, 8
- Kim, J.-h., Abel, T., Agertz, O., et al. 2014, *ApJS*, **210**, 14
- Kim, J.-h., Agertz, O., Teyssier, R., et al. 2016, *ApJ*, **833**, 202
- Kirby, E. N., Martin, C. L., & Finlator, K. 2011, *ApJL*, **742**, L25
- Klypin, A., Kravtsov, A. V., Valenzuela, O., & Prada, F. 1999, *ApJ*, **522**, 82
- Kobayashi, C. 2004, *MNRAS*, **347**, 740
- Kobayashi, C., Tsujimoto, T., & Nomoto, K. 2000, *ApJ*, **539**, 26
- Kroupa, P., Weidner, C., Pflamm-Altenburg, J., et al. 2013, The Stellar and Sub-Stellar Initial Mass Function of Simple and Composite Populations, ed. T. D. Oswalt & G. Gilmore, 115
- Krumholz, M. R. 2013, *MNRAS*, **436**, 2747
- Krumholz, M. R., Klein, R. I., & McKee, C. F. 2007, *ApJ*, **656**, 959
- Krumholz, M. R., McKee, C. F., & Klein, R. I. 2004, *ApJ*, **611**, 399
- Krumholz, M. R., & Thompson, T. A. 2012, *ApJ*, **760**, 155
- Lanz, T., & Hubeny, I. 2003, *ApJS*, **146**, 417
- Leitherer, C., Robert, C., & Drissen, L. 1992, *ApJ*, **401**, 596
- Leroy, A. K., Walter, F., Brinks, E., et al. 2008, *AJ*, **136**, 2782
- Leroy, A. K., Walter, F., Sandstrom, K., et al. 2013, *AJ*, **146**, 19
- Lia, C., Portinari, L., & Carraro, G. 2002, *MNRAS*, **330**, 821
- Ma, X., Hopkins, P. F., Faucher-Giguère, C.-A., et al. 2016a, *MNRAS*, **456**, 2140
- Ma, X., Hopkins, P. F., Kasen, D., et al. 2016b, *MNRAS*, **459**, 3614
- Mac Low, M.-M., & Ferrara, A. 1999, *ApJ*, **513**, 142
- Majewski, S. R., APOGEE Team, & APOGEE-2 Team. 2016, *Astronomische Nachrichten*, **337**, 863
- Majewski, S. R., Wilson, J. C., Hearty, F., Schiavon, R. R., & Skrutskie, M. F. 2010, in IAU Symposium, Vol. 265, Chemical Abundances in the Universe: Connecting First Stars to Planets, ed. K. Cunha, M. Spite, & B. Barbuy, 480
- Maoz, D., Mannucci, F., & Nelemans, G. 2014, *ARA&A*, **52**, 107
- Maoz, D., Sharon, K., & Gal-Yam, A. 2010, *ApJ*, **722**, 1879
- Marcolini, A., D’Ercole, A., Battaglia, G., & Gibson, B. K. 2008, *MNRAS*, **386**, 2173
- McQuinn, K. B. W., Skillman, E. D., Dalcanton, J. J., et al. 2012, *ApJ*, **751**, 127
- McQuinn, K. B. W., Skillman, E. D., Berg, D., et al. 2013, *AJ*, **146**, 145
- McQuinn, K. B. W., Skillman, E. D., Dolphin, A., et al. 2015a, *ApJ*, **812**, 158
- . 2015b, *ApJL*, **815**, L17
- Momose, R., Koda, J., Kennicutt, Jr., R. C., et al. 2013, *ApJL*, **772**, L13
- Moore, B., Ghigna, S., Governato, F., et al. 1999, *ApJL*, **524**, L19
- Muratov, A. L., Kereš, D., Faucher-Giguère, C.-A., et al. 2015, *MNRAS*, **454**, 2691
- . 2017, *MNRAS*, **468**, 4170
- Naab, T., & Ostriker, J. P. 2016, ArXiv e-prints, [arXiv:1612.06891](https://arxiv.org/abs/1612.06891)
- Obreja, A., Brook, C. B., Stinson, G., et al. 2014, *MNRAS*, **442**, 1794
- Ocvirk, P., Gillet, N., Shapiro, P. R., et al. 2016, *MNRAS*, **463**, 1462
- Offner, S. S. R., & Arce, H. G. 2015, *ApJ*, **811**, 146
- Oh, S.-H., de Blok, W. J. G., Brinks, E., Walter, F., & Kennicutt, Jr., R. C. 2011, *AJ*, **141**, 193
- Omukai, K. 2000, *ApJ*, **534**, 809
- Omukai, K., Tsuribe, T., Schneider, R., & Ferrara, A. 2005, *ApJ*, **626**, 627
- Oppenheimer, B. D., & Davé, R. 2006, *MNRAS*, **373**, 1265
- . 2008, *MNRAS*, **387**, 577
- Oppenheimer, B. D., Crain, R. A., Schaye, J., et al. 2016, *MNRAS*, **460**, 2157
- Orr, M., Hayward, C., Hopkins, P., et al. 2017, ArXiv e-prints, [arXiv:1701.01788](https://arxiv.org/abs/1701.01788)
- Pakmor, R., Pfrommer, C., Simpson, C. M., & Springel, V. 2016, *ApJL*, **824**, L30
- Parravano, A., Hollenbach, D. J., & McKee, C. F. 2003, *ApJ*, **584**, 797
- Pawlak, A. H., Milosavljević, M., & Bromm, V. 2013, *ApJ*, **767**, 59
- Pawlak, A. H., Rahmati, A., Schaye, J., Jeon, M., & Dalla Vecchia, C. 2017, *MNRAS*, **466**, 960
- Peeples, M. S., Werk, J. K., Tumlinson, J., et al. 2014, *ApJ*, **786**, 54
- Peters, T., Naab, T., Walch, S., et al. 2017, *MNRAS*, **466**, 3293
- Pflamm-Altenburg, J., & Kroupa, P. 2006, *MNRAS*, **373**, 295
- Pignatari, M., Herwig, F., Hirschi, R., et al. 2016, *ApJS*, **225**, 24
- Puls, J., Springmann, U., & Lennon, M. 2000, *A&AS*, **141**, 23
- Rahmati, A., Pawlik, A. H., Raičević, M., & Schaye, J. 2013, *MNRAS*, **430**, 2427
- Rémy-Ruyer, A., Madden, S. C., Galliano, F., et al. 2014, *A&A*, **563**, A31
- Renaud, F., Bournaud, F., Emsellem, E., et al. 2013, *MNRAS*, **436**, 1836
- Revaz, Y., Arnaudon, A., Nichols, M., Bonvin, V., & Jablonka, P. 2016, ArXiv e-prints, [arXiv:1601.02017](https://arxiv.org/abs/1601.02017)
- Revaz, Y., & Jablonka, P. 2012, *A&A*, **538**, A82
- Revaz, Y., Jablonka, P., Sawala, T., et al. 2009, *A&A*, **501**, 189
- Ritter, C., Herwig, F., Jones, S., et al. 2017, ArXiv e-prints, [arXiv:1709.08677 \[astro-ph.SR\]](https://arxiv.org/abs/1709.08677)
- Roederer, I. U., Cowan, J. J., Preston, G. W., et al. 2014, *MNRAS*, **445**, 2970
- Romeo, A. D., Portinari, L., & Sommer-Larsen, J. 2005, *MNRAS*, **361**, 983

- Rosdahl, J., Schaye, J., Teyssier, R., & Agertz, O. 2015, *MNRAS*, **451**, 34
- Roškar, R., Teyssier, R., Agertz, O., Wetzel, M., & Moore, B. 2014, *MNRAS*, **444**, 2837
- Roychowdhury, S., Chengalur, J. N., Begum, A., & Karachentsev, I. D. 2009, *MNRAS*, **397**, 1435
- Roychowdhury, S., Chengalur, J. N., Kaisin, S. S., & Karachentsev, I. D. 2014, *MNRAS*, **445**, 1392
- Roychowdhury, S., Chengalur, J. N., & Shi, Y. 2017, ArXiv e-prints, [arXiv:1708.02298](#)
- Ruszkowski, M., Yang, H.-Y. K., & Zweibel, E. 2017, *ApJ*, **834**, 208
- Salaris, M., Serenelli, A., Weiss, A., & Miller Bertolami, M. 2009, *ApJ*, **692**, 1013
- Salem, M., Besla, G., Bryan, G., et al. 2015, *ApJ*, **815**, 77
- Salem, M., & Bryan, G. L. 2014, *MNRAS*, **437**, 3312
- Salem, M., Bryan, G. L., & Corlies, L. 2016, *MNRAS*, **456**, 582
- Salem, M., Bryan, G. L., & Hummels, C. 2014, *ApJL*, **797**, L18
- Salpeter, E. E. 1955, *ApJ*, **121**, 161
- Sand, D. J., Crnojević, D., Bennet, P., et al. 2015, *ApJ*, **806**, 95
- Sawala, T., Scannapieco, C., Maio, U., & White, S. 2010, *MNRAS*, **402**, 1599
- Schaye, J., Dalla Vecchia, C., Booth, C. M., et al. 2010, *MNRAS*, **402**, 1536
- Schaye, J., Crain, R. A., Bower, R. G., et al. 2015, *MNRAS*, **446**, 521
- Schruba, A., Leroy, A. K., Kruijssen, J. M. D., et al. 2017, *ApJ*, **835**, 278
- Shen, S., Madau, P., Guedes, J., et al. 2013, *ApJ*, **765**, 89
- Shen, S., Wadsley, J., & Stinson, G. 2010, *MNRAS*, **407**, 1581
- Shi, Y., Helou, G., Yan, L., et al. 2011, *ApJ*, **733**, 87
- Simpson, C. M., Pakmor, R., Marinacci, F., et al. 2016, *ApJL*, **827**, L29
- Skillman, E. D., Salzer, J. J., Berg, D. A., et al. 2013, *AJ*, **146**, 3
- Smith, B., Sigurdsson, S., & Abel, T. 2008, *MNRAS*, **385**, 1443
- Smith, B. D., Bryan, G. L., Glover, S. C. O., et al. 2017, *MNRAS*, **466**, 2217
- Snaith, O., Haywood, M., Di Matteo, P., et al. 2015, *A&A*, **578**, A87
- Somerville, R. S., & Davé, R. 2015, *ARA&A*, **53**, 51
- Sormani, M. C., Treß, R. G., Klessen, R. S., & Glover, S. C. O. 2017, *MNRAS*, **466**, 407
- Stinson, G. S., Bailin, J., Couchman, H., et al. 2010, *MNRAS*, **408**, 812
- Stinson, G. S., Brook, C., Macciò, A. V., et al. 2013, *MNRAS*, **428**, 129
- Su, K.-Y., Hopkins, P. F., Hayward, C. C., et al. 2017, *MNRAS*, **471**, 144
- Tang, J., Bressan, A., Rosenfield, P., et al. 2014, *MNRAS*, **445**, 4287
- Teich, Y. G., McNichols, A. T., Nims, E., et al. 2016, *ApJ*, **832**, 85
- Thielemann, F.-K., Nomoto, K., & Yokoi, K. 1986, *A&A*, **158**, 17
- Tollerud, E. J., Geha, M. C., Grcevich, J., Putman, M. E., & Stern, D. 2015, *ApJL*, **798**, L21
- Tonnesen, S., & Bryan, G. L. 2009, *ApJ*, **694**, 789
- Tornatore, L., Borgani, S., Matteucci, F., Recchi, S., & Tozzi, P. 2004, *MNRAS*, **349**, L19
- Truelove, J. K., Klein, R. I., McKee, C. F., et al. 1997, *ApJL*, **489**, L179
- Turk, M. J., Smith, B. D., Oishi, J. S., et al. 2011, *ApJS*, **192**, 9
- Ugliano, M., Janka, H.-T., Marek, A., & Arcones, A. 2012, *ApJ*, **757**, 69
- Verner, D. A., Ferland, G. J., Korista, K. T., & Yakovlev, D. G. 1996, *ApJ*, **465**, 487
- Vink, J. S., & de Koter, A. 2005, *A&A*, **442**, 587
- Vogelsberger, M., Genel, S., Springel, V., et al. 2014, *MNRAS*, **444**, 1518
- Vorobyov, E. I., Recchi, S., & Hensler, G. 2015, *A&A*, **579**, A9
- Walter, F., Brinks, E., de Blok, W. J. G., et al. 2008, *AJ*, **136**, 2563
- Weaver, R., McCray, R., Castor, J., Shapiro, P., & Moore, R. 1977, *ApJ*, **218**, 377
- Weidner, C., & Kroupa, P. 2004, *MNRAS*, **348**, 187
- Wiener, J., Pfrommer, C., & Peng Oh, S. 2017, *MNRAS*, **467**, 906
- Wiersma, R. P. C., Schaye, J., Theuns, T., Dalla Vecchia, C., & Tornatore, L. 2009, *MNRAS*, **399**, 574
- Wise, J. H., & Abel, T. 2011, *MNRAS*, **414**, 3458
- Wise, J. H., Abel, T., Turk, M. J., Norman, M. L., & Smith, B. D. 2012a, *MNRAS*, **427**, 311
- Wise, J. H., Demchenko, V. G., Halicek, M. T., et al. 2014, *MNRAS*, **442**, 2560
- Wise, J. H., Turk, M. J., Norman, M. L., & Abel, T. 2012b, *ApJ*, **745**, 50
- Wolcott-Green, J., Haiman, Z., & Bryan, G. L. 2011, *MNRAS*, **418**, 838
- Wolfire, M. G., McKee, C. F., Hollenbach, D., & Tielens, A. G. G. M. 2003, *ApJ*, **587**, 278
- Woosley, S. E., Heger, A., & Weaver, T. A. 2002, *Reviews of Modern Physics*, **74**, 1015
- Zahid, H. J., Dima, G. I., Kewley, L. J., Erb, D. K., & Davé, R. 2012, *ApJ*, **757**, 54
- Zhang, D., & Davis, S. W. 2017, *ApJ*, **839**, 54
- Zhang, W., Woosley, S. E., & Heger, A. 2008, *ApJ*, **679**, 639
- Zheng, Y. 2017, Mapping Gas Flows from the Disk to the Circumgalactic Medium, HST Proposal
- Zheng, Y., Peek, J. E. G., Werk, J. K., & Putman, M. E. 2017, *ApJ*, **834**, 179

APPENDIX

A. GAS PHASES OF THE ISM

To aid in comparison to other works, we define our ISM phases here, as adopted from Draine (2011) Table 1.3 and used consistently throughout this analysis. By construction, these phases are mutually exclusive. In the below, f_{H_2} is the molecular hydrogen fraction by abundance.

1. Hot Ionized Medium (HIM): $T \geq 10^{5.5} \text{ K}$
2. Warm Ionized Medium (WIM): $10^4 \text{ K} \leq T < 10^{5.5} \text{ K}$
3. Warm Neutral Medium (WNM): $10^2 \text{ K} \leq T < 10^4 \text{ K}$
4. Cold Neutral Medium (CNM): $T < 10^2 \text{ K}$, $f_{\text{H}_2} \leq 0.5$
5. Molecular: **MAY CHANGE** $T < 10^2 \text{ K}$, $f_{\text{H}_2} > 0.5$

B. STELLAR RADIATION PROPERTIES

We detail the radiation properties of our model stars as a function of stellar mass and metallicity, both of which are assigned directly from an IMF and from the local gas properties respectively. The stellar radiation properties are determined from the OSTAR2002 grid (Lanz & Hubeny 2003) (or as integrated from an adjusted black body curve for stars off of the OSTAR2002 grid) given the ZAMS stellar radius obtained from the PARSEC (Bressan et al. 2012; Tang et al. 2014) stellar evolution data set. In Figure 15 we plot the ionizing photon luminosities for HI (top left) and HeI (top right) for each star, the FUV (middle left) and LW (middle right) luminosities, and finally the HI ionizing radiation photon energy (bottom left) and HeI ionizing photon energy (bottom right). We use a constant factor across metallicities for stars not sampled on the OSTAR2002 grid to shift the black body radiation fluxes to be roughly continuous with the ionizing photon rates and luminosities as a function of stellar mass. This requires two factors for each radiation type, one for low mass and one for high mass stars. We use the following multiplicative factors to adjust the black body spectrum for HI and HeI radiation respectively: [0.1, 3.2] and [0.0001, 4.0]. We do not find this adjustment to be necessary for the FUV and LW radiation bands.

The ionizing radiation photon energies are taken as the average ionizing photon energy for a black body of the star's given T_{eff} obtained from the PARSEC grid. A more accurate approach to compute this energy would convolve the full stellar spectrum and the frequency dependent absorption cross section. We tested this approach using the frequency dependent photoionization cross sections from Verner et al. (1996).¹⁰ The black body approximation is accurate to within 5%, yet substantially easier to compute on the fly as integrals over the black body spectrum can be expressed as infinite series that rapidly converge to high precision. Unlike the ionizing radiation, we assume constant FUV and LW band energies for each star, at 9.8 eV and 12.8 eV respectively.

C. TYPICAL GAS DENSITIES IN SUPERNOVA INJECTION REGIONS

Modeling supernova feedback with the injection of thermal energy alone can lead to rapid over cooling of the injected energy, and a significant underestimate of the effects of supernova feedback. Often, ad hoc solutions to this problem are used in large simulations with coarse resolution, such as momentarily turning off cooling in feedback affected regions or decoupling affected regions from the hydrodynamics for some time. However, physically consistent solutions have been employed (e.g Simpson et al. 2016) which inject a mixture of kinetic and thermal energy, whose ratio of kinetic to thermal energy injection depends on resolution and/or local gas density. This over cooling problem improves with higher resolution and lower ISM densities, until eventually pure thermal energy injection is sufficient to resolve each supernova. We take advantage of our high ($\sim \text{pc}$) scale resolution and employ a simple thermal energy injection model for our supernova feedback. Here we demonstrate how well this resolves our supernovae in the comparison simulation presented in this work.

The left panel of Figure 16 gives the distributions of the max (orange) and average (black) ISM number densities in the supernova injection regions for each supernovae in the simulations presented in this work. As shown, a majority explode in regions at substantially lower densities than the star formation threshold of 200 cm^{-3} . For most supernovae, $n_{\text{max}} \leq 1.0 \text{ cm}^{-3}$, which is due to the substantial pre-supernova feedback included in our simulations. The right panel of Figure 16 gives the

¹⁰ Source code containing the analytic fits given in Verner et al. (1996) was obtained from <http://www.pa.uky.edu/~verner/photo.html>

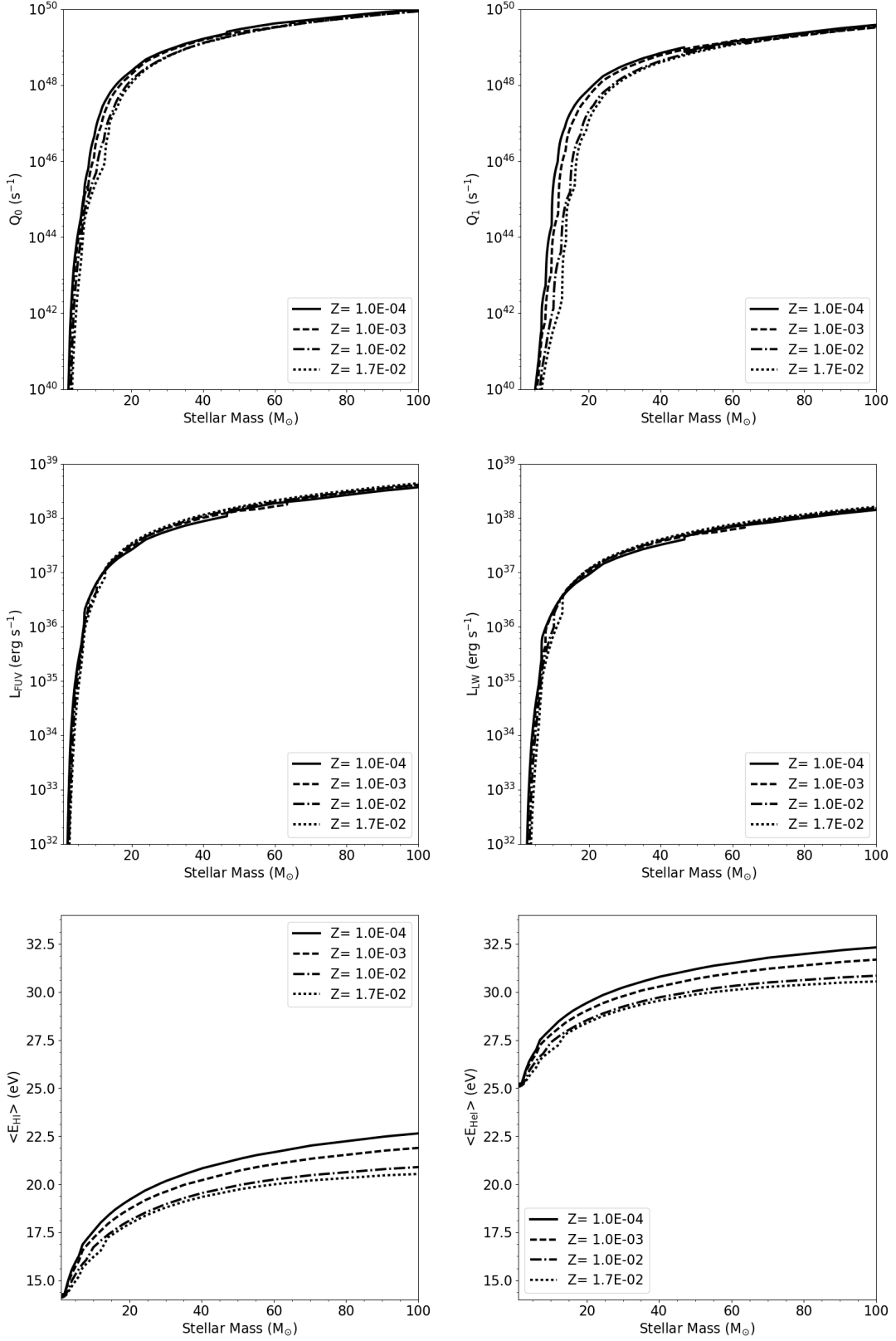


Figure 15. Radiation properties for our model stars. Note, we only track radiation from stars above $8.0 M_\odot$, which dominate over less massive stars, even when accounting for IMF weighting.

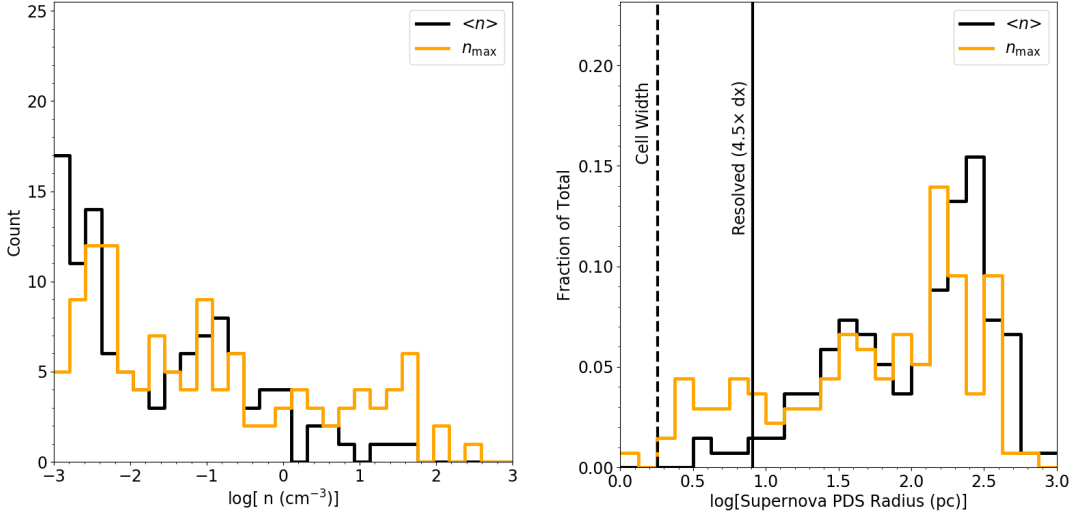


Figure 16. Distribution of peak and average gas densities (left) in the injection region of each of the supernovae from the simulation. On the right, we give the distribution of the radius of the pressure driven snowplow phase for each supernova assuming a uniform medium at either the peak or average density in the injection region. The vertical lines give one and 4.5 cell widths. As shown, a fraction of these SN are certainly under resolved, with R_{PDS} less than a single cell size, but a majority are resolved.

fractional distribution of the calculated radius of pressure driven snowplow (R_{PDS}) phase of the Sedov-Taylor expansion, adopting the definitions from [Simpson et al. \(2016\)](#), given as

$$R_{\text{PDS}} = \begin{cases} 49.3 E_{51}^{1/4} n_o^{-1/2} & \text{if } Z \leq 0.01 \\ 18.5 E_{51}^{2/7} n_o^{-3/7} Z^{-1/7} & \text{if } Z \geq 0.01 \end{cases}$$

where E_{51} is the injection energy in units of 10^{51} erg, n_o is the number density of the medium, and Z is the metallicity in units of Z_\odot . [Simpson et al. \(2016\)](#) found that $R_{\text{PDS}} > 4.5 \Delta x$ is needed to resolve the supernova explosion with thermal energy injection alone, assuming uniform density in the injection region. In practice, the injection region is never uniform. We give R_{PDS} assuming uniform density at both the average and maximum number density in the injection region of each supernova. As shown, a majority of supernovae are resolved (to the right of the $4.5 \Delta x$ line), but that up to 10% are somewhat under-resolved. In general, these are supernova explosions from the most massive (i.e. most prompt) stars. We do not expect that resolving these supernovae will dramatically alter our results, but note that simulations presented in future work will examine lower mass galaxies at higher resolution than those presented here. In those, the supernovae are more resolved, but we note that using our feedback model at resolutions much less than 2 pc will require adopting a different injection mechanism.

D. COOLING RATES

Figure 17 shows the combined primordial and metal line cooling (dashed) and heating (dotted) rates at three characteristic densities for $Z = 0.01 Z_\odot$, closer to the metallicities of our fiducial set of dwarf galaxy simulations (Emerick et. al. in prep). The solid lines give the absolute value of the net cooling rate, which more clearly indicates the regime at low temperatures where heating dominates. The curve as shown includes the $z = 0$ [Haardt & Madau \(2012\)](#) metagalactic UVB.

We note that this cooling curve shows only an approximation of the local cooling and heating rates used in the simulations for two reasons. First, the primordial cooling and heating rates shown here are those returned by CLOUDY, but only the tabulated CLOUDY metal line cooling and heating rates are used. The actual primordial heating and cooling rates are calculated self-consistently using the non-equilibrium chemistry solver and the self-shielding approximation from radiative transfer simulations given in [Rahmati et al. \(2013\)](#). However, given that we remove the optically thin assumption when computing the CLOUDY tables, the rates shown should be comparable to the locally varying cooling curve in the simulations. Second, this figure ignores the contributions to the heating rate from the variable interstellar radiation field, namely the stellar contribution to photoelectric heating, heating from LW dissociation, and ionization heating. We describe how we obtain the metal line cooling rates below and quantify the change in using these updated tables.

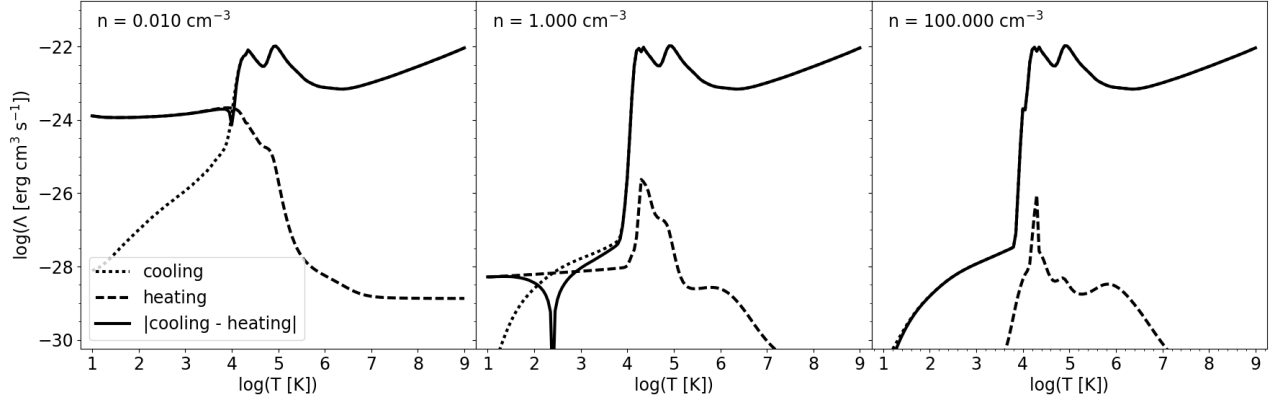


Figure 17. The total heating and cooling rates extracted from the core of a Jeans-length sized cloud irradiated by a Haardt & Madau (2012) metagalactic background as modeled in CLOUDY. The absolute value of the net cooling rate is shown with solid lines.

The cooling curves used in this work corrects a significant conceptual inconsistency one may encounter when using tabulated metal line cooling rates in combination with self-shielding approximations. Previous work in Hu et al. (2017) details this inconsistency. In short, adopting tabulated metal cooling rates computed under the assumption of an optically thin UV background overestimates the electron fraction in regimes where self-shielding is important, about $-0.5 \leq \log(n [\text{cm}^{-3}]) < 2$, leading to an overestimation of the metal cooling rates. We demonstrate this effect in Figure 18, which gives $|\text{cooling} - \text{heating}|$ for our full model at $Z = 0.1 Z_{\odot}$ (black) as compared to a model using the optically thin metal line cooling rates (orange) at a range of densities. The effect is most significant at moderate densities, where the net cooling rate can be an order of magnitude higher. In low temperature regions, this can significantly shift the inferred equilibrium temperature.

The cooling curve shown in Figure 17 avoids this discrepancy using re-computed metal line cooling tables. We have made these tables publicly available in the main distribution of Grackle. For densities where self-shielding is important, we computed Cloudy models of 1D clouds at each temperature and density pair with a physical size corresponding to the Jeans length. In cases where the Jeans length is very large, we limit the size to 100 pc, a reasonable approximation for the maximum size of a self-gravitating cloud. We then adopt the metal line cooling rates obtained from the center of these clouds, whose outside is exposed to the UVB. These models were computed with a modified version of the CIAOLoop¹¹ code used in Smith et al. (2008). In computing these tables we had to include the CR ionization that dominates in optically thick clouds. Without this effect, Cloudy becomes unstable in entirely neutral regions. We adopted a CR ionization rate of 10% the MW value, though we note varying this from 1% to 100% the MW value did not have an effect on the extracted metal line cooling rates.

E. RESOLUTION STUDY

Insert some light resolution study details here. Ultimately this will be somewhat difficult as we need to go into how this is challenging since star formation criteria will change as resolution scales.

¹¹ https://bitbucket.org/brittonsmith/cloudy_cooling_tools (our version: https://github.com/aemerick/cloudy_tools)

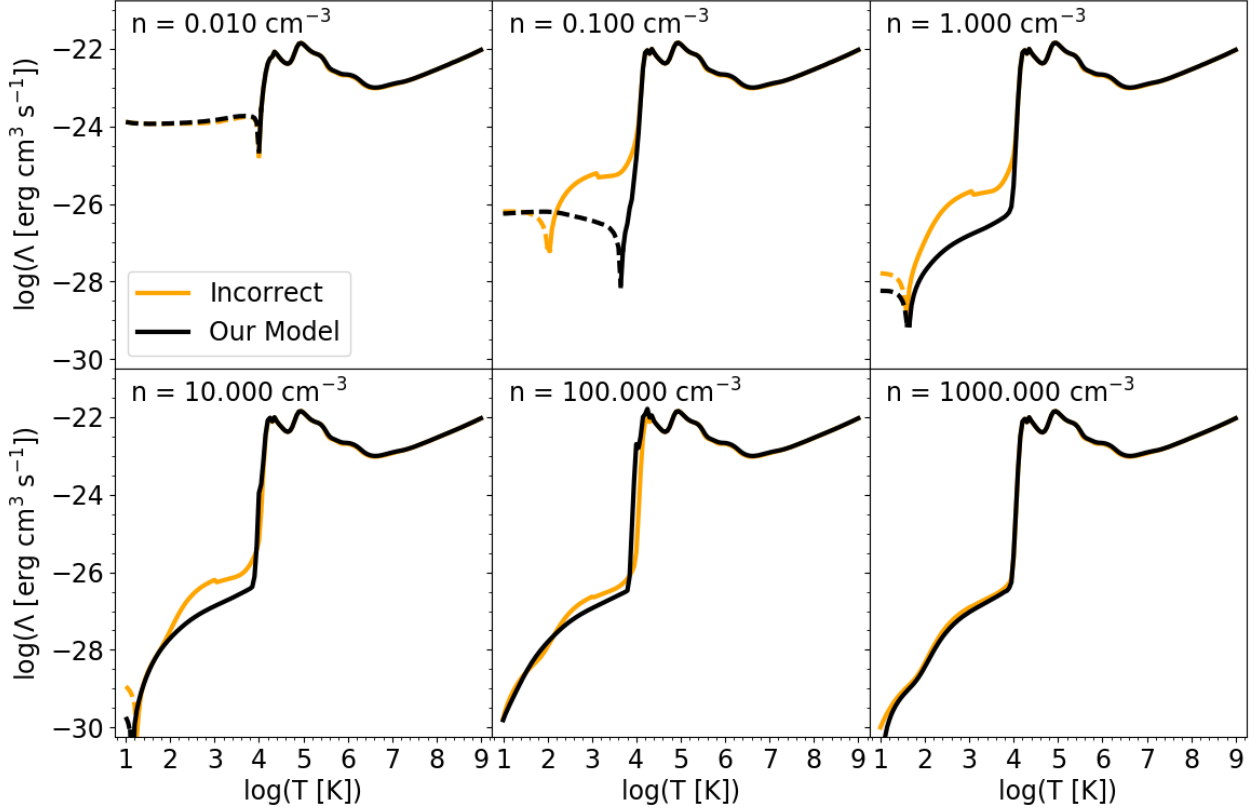


Figure 18. The absolute value of the net cooling rate ($|\text{cooling} - \text{heating}|$) in two models that account for self-shielding of primordial gas against a metagalactic UV background. Our model (black) uses self-consistent metal line cooling rates, and is compared to an incorrect model (orange) that adopts the un-corrected (i.e. optically thin) metal line cooling rates. The regimes where heating dominates are plotted with dashed lines for clarity.